




Intercomparing Superconducting Gravimeter Records in a Dense Meter-Scale Network at the J9 Gravimetric Observatory of Strasbourg, France

J. HINDERER,¹  R. J. WARBURTON,² S. ROSAT,¹ U. RICCARDI,³ J.-P. BOY,¹ F. FORSTER,⁴ P. JOUSSET,⁴ A. GÜNTNER,⁴ K. ERBAS,⁴ F. LITTEL,¹ and J.-D. BERNARD¹

Abstract—This study is a metrological investigation of eight superconducting gravimeters that have operated in the Strasbourg gravimetric Observatory. These superconducting gravimeters include an older compact C026 model, a new observatory type iOSG23 and six iGravs (6, 15, 29, 30, 31, 32). We first compare the amplitude calibration of the meters using measurements from FG5 #206 absolute gravimeter (AG). In a next step we compute the amplitude calibration of all the meters by time regression with respect to iOSG23 itself carefully calibrated by numerous AG experiments. The relative calibration values are much more precise than absolute calibration for each instrument and strongly reduce any tidal residual signal. We also compare the time lags of the various instruments with respect to iOSG23, either by time cross-correlation or tidal analysis for the longest records (about 1 year). The instrumental drift behavior of the iGravs and iOSG23 is then investigated and we examine the relationships observed between gravity and body temperature measurements. Finally, we compare the noise levels of all the instruments. A three-channel correlation analysis is used to separate the incoherent (instrumental) noise from the coherent (ambient) noise. The self-noise is then compared to a model of thermal noise (Brownian motion) using the known instrumental parameters of the damped harmonic oscillator. The self-noise of iGrav instruments is well-explained by the thermal noise model at seismic frequencies (between 10^{-3} and 10^{-2} Hz). As expected, the self-noise of iOSG23 with a heavier sphere is also lower than that of iGravs at such frequencies.

Keywords: Superconducting gravimeter, levitation, calibration, instrumental drift, noise.

1. Introduction

Eight different superconducting gravimeters (SG) manufactured by GWR Instruments, Inc. have been operated at J9 gravimetric Observatory of Strasbourg. A compact C026 was the first SG installed in 1996, an iOSG-type (#23) in January 2016 and iGrav (#29) in July 2016, and five other iGrav-type (#6, #15, #30, #31, #32) at various intervals. Figure 1 shows the three different types of SG used in this intercomparison study.

The C026 was installed in July 1996 and proved to have very good time-stability (Calvo et al., 2014, 2017; Riccardi et al., 2009) and good performances in terms of noise levels (Rosat & Hinderer, 2011) enabling the study of very long-period geophysical phenomena and the analysis of small tidal constituents (e.g. Calvo et al., 2016). Experiences of intercomparison and validation tests of spring gravimeters, conducted in the past at J9, have benefited from the stability of the C026 and the low noise level in the observatory (Arnosó et al., 2014). Since February 2016 the iOSG23 (see below) operated next to the C026 (Boy et al., 2017; <http://doi.org/10.5880/igets.st.11.001>). C026 had experienced many problems due to its very old electronics (more than 25 years old) and was turned off in November 2018. The C026 data were also not usable between November 2016 and April 2017 because of a failure of the data acquisition system.

The latest generation of single-sphere SGs are the iGrav and the iOSG using identical sensors, electronics and refrigeration systems. The iOSG uses a heavier sphere (17.7 g versus 4.3 g) and has a larger dewar (35 L versus 16 L) and consequently has a

¹ Institut Terre et Environnement de Strasbourg (UMR 7063), Université de Strasbourg/EOST, CNRS, Strasbourg, France. E-mail: jhinderer@unistra.fr

² GWR Instruments Inc., San Diego, USA.

³ Dipartimento di Scienze della Terra, dell'Ambiente e delle Risorse (DiSTAR), Università Federico II di Napoli, Naples, Italy.

⁴ Helmholtz-Zentrum Potsdam, Deutsches GeoForschungsZentrum GFZ, Potsdam, Germany.

slightly lower instrumental noise level and a longer hold time during power failures. In contrast, the iGrav, which was designed for field use, is easier to move and operate at remote sites (Warburton et al., 2011). The iOSG23 was installed at J9 in January 2016 and is the second iOSG installed in France; the first one was iOSG24 installed in July 2015 at the low background noise interdisciplinary ground and underground based research laboratory LSBB of Rustrel, in the south of France (Rosat et al., 2016). Only three iOSGs have been manufactured and the third, iOSG22, was installed at Metsähovi Geodetic Fundamental Research Station (ME), Finland in December 2016. The older compact C026 was a second generation of SG manufactured between 1994 and 2002 with a 125 L dewar. The iOSG and iGrav instruments use SHI RKD 101 refrigerating systems to cool below 4 Kelvin and condense helium gas (He) to liquid inside the dewar so that there is no He loss and no need to transfer liquid He. In contrast, the C026 used an older APD Cryogenics DE202A cold-head with only 9 K cooling capability so He gas boils off slowly. As a result, the C026 required regular human intervention (about every 10 months) to refill the dewar with liquid He.

iGrav29, iGrav30 and iGrav31 were purchased in 2016 in the framework of the Equipex CRITEX recently integrated in OZCAR (<https://www.ozcar-ri.org/ozcar/>), which is the French network of Critical Zone Observatories (Gaillardet et al., 2018). The iGravs are one type of equipment for this hydrology-

oriented project dedicated to the gravity monitoring of basin catchment and the study of the critical zone. These three iGravs were installed at J9 in July 2016. After operation at J9, iGrav30 was moved to the Strengbach catchment in the Vosges mountains (at 70 km from Strasbourg) end of June 2017 and iGrav31 was moved in May 2019 to the surface station at LSBB (<https://lsbb.cnrs.fr>) in South of France. iGrav30 is used to investigate the water storage changes at the catchment scale (Chaffaut et al., 2020), while iGrav31 establishes together with iOSG24 (the twin meter of iOSG23 studied here) a differential gravity experiment that will be very useful to locate the underground water mass changes already detected by iOSG24 alone (Mouyen et al., 2019; Rosat et al., 2016, 2018). The eight SGs were installed in different rooms of the J9 bunker as illustrated in Fig. 2.

iGrav6, iGrav15, and iGrav32 were moved to the Strasbourg Observatory by German colleagues for a validation test in 2017 before being sent to Iceland in the frame of the “Microgravimotis” project for gravity monitoring of the Theistareykir geothermal site (Erbaş et al., 2019). The performances of these 3 iGravs after transportation to Iceland are investigated in Schäfer et al. (2020). As can be seen in the timetable (Fig. 3), end of August 2017 iGrav32 had to be sent back to the manufacturer GWR for instrumental upgrade and did come back to J9 only for a short time in October 2017; the period before the upgrade refers to 32a and after upgrade 32b.



Figure 1

A picture showing the types of SGs operating side by side and their physical installations in the J9 Observatory near Strasbourg (France): from left to right, C026 on a large isolated pillar; iOSG23 straddling a small isolated pillar; iGrav32 operating directly on the concrete floor; and iGrav30 with coldhead frame modified to fit on a small isolated pillar

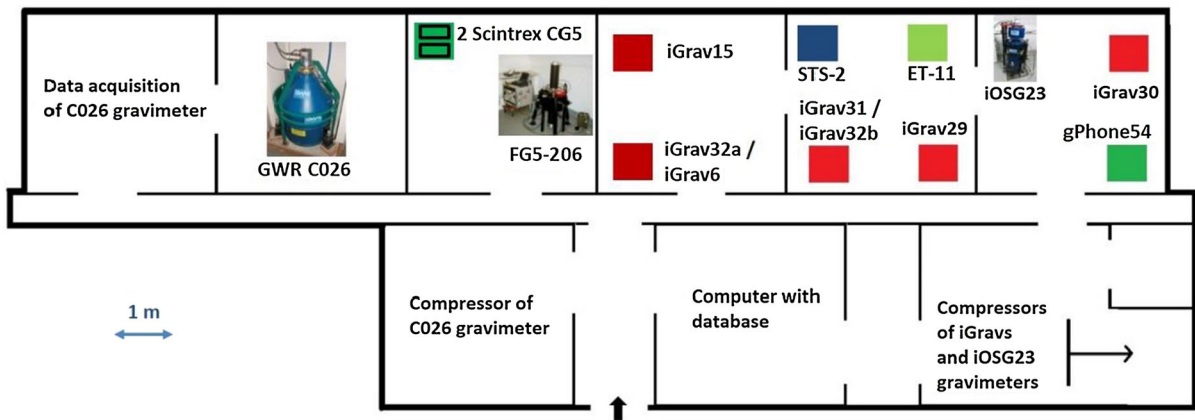


Figure 2

Floor plan of the Strasbourg Gravimetric Observatory (J9) indicating the location of the various instruments that are compared in this study

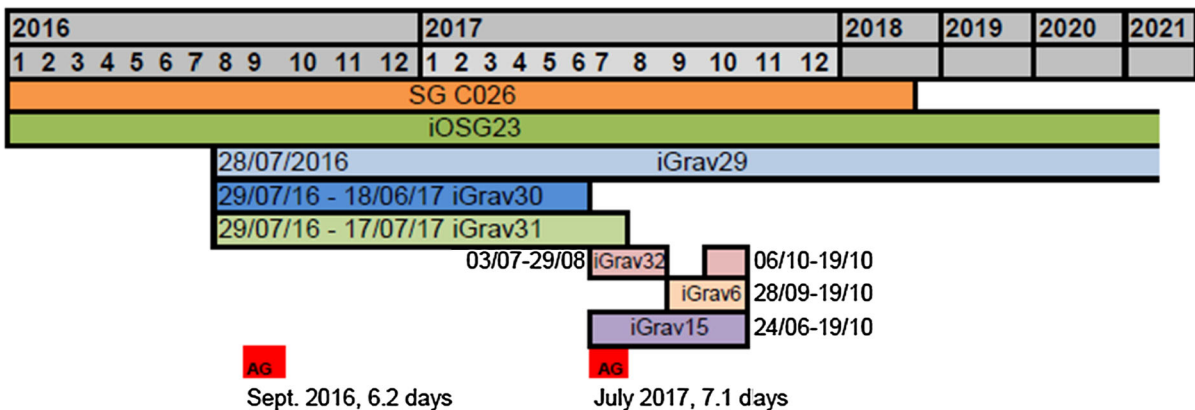


Figure 3

Timetable of the SG and AG measurements in the J9 Observatory

iGrav6 also came only for limited time end of September 2017 before shipment to Iceland.

For both historical reasons and convenience, a variety of methods as shown in Fig. 1 were used to physically set SGs at J9. C026 was operated in its own room and on a wide and deep pillar (0.8 m × 0.8 m × 2 m) isolated from the floor that was originally built for operating one of the early GWR TT70 SGs. Two of the rooms at J9 have small isolated pillars (0.6 m × 0.6 m × 0.6 m) previously used for testing LaCoste and Romberg, Scintrex and gPhone gravity meters. Although the base of the iOSG23 dewar fits on the small pillar, its coldhead isolation frame does not. Therefore, the coldhead isolation frame straddles the pillar with two of its feet on the pillar and one on the nearby concrete floor.

iGravs 29, 30, 31 and 32b were also operated on small pillars; however, for these iGravs, the connecting angles of the legs to the coldhead support bracket were decreased during installation to reduce their footprints to fit onto the small pillars. The iGrav15, iGrav6 and iGrav32a were installed directly on the concrete ground without any modification to their coldhead frames. As a consequence, some differences between the physical installations for the eight instruments could influence the measured noise levels between them.

The timetable showing the available data sets is given in Fig. 3. The maximum number of SGs measuring simultaneously in our study is six because there is no overlap between iGrav30 that left the

Table 1
Results for absolute calibration of SGs using SG/AG parallel records; V stands for Volt

SG name	Length of calibration	Absolute calibration and error (nm/s ² /V)	Dimensionless error (%)
C026	Numerous experiments with FG5#206 during 1996–2018	$- 792 \pm 1$	0.1
iOSG23	6.2 days	$- 451 \pm 2$	0.4
iGrav15	7.1 days	$- 934 \pm 3$	0.3
iGrav29	6.2 days	$- 940 \pm 4$	0.4
iGrav30	6.2 days	$- 918 \pm 4$	0.4
iGrav31	6.2 days	$- 853 \pm 4$	0.5
iGrav32	7.1 days	$- 898 \pm 3$	0.3

Observatory for a remote installation before iGrav32 arrived.

In this paper, we compare the accuracy and precision of the time variations of gravity recorded by the various SGs. We start by first testing the precision of the scaling factors used to calibrate the SGs and we estimate the time delays (phase lags) between the instruments, either by directly comparing the time series and their correlation, or by using tidal admittances obtained from tidal analyses. Next, the instrumental drift is carefully investigated, particularly the initial drift subsequent to the installation of each gravimeter. And finally, from the few months of parallel records, we finally use a standard procedure to compute power spectral densities (PSDs) using the Welch's overlapped segment averaging estimator in order to give reference noise levels for these instruments. These PSDs are compared with the seismological reference noise models and with other relative mechanical gravimeters and a long-period seismometer that have been recorded at J9. Self-noise levels are also estimated and compared with a predicted thermal noise model.

2. Amplitude Calibration and Time Delay

2.1. Absolute Calibration

SGs are relative instruments that need to be calibrated using an absolute reference. Since the transfer function of the SGs is flat at frequencies much lower than Nyquist frequency (0.5 Hz), the calibration is usually achieved by estimating a scale

factor with tides recorded by parallel co-located absolute gravity measurements performed with a FG5 ballistic instrument (Fukuda et al., 2005; Hinderer et al., 1991; Imanishi et al., 2002; Tamura et al., 2004). Following recent papers (Crossley et al., 2018; Meurers, 2012; Van Camp et al., 2015), we used parallel FG5 drop measurements to which a L1-norm adjustment of the low-pass filtered SG data decimated to 10 s is performed. This L1-normalization is used in order to avoid the influence of outliers. The FG5 drop standard deviations are considered in the fitting process. Scale factors obtained in this way (absolute calibration factors) are summarized in Table 1 as well as the time periods during which the various instruments were recording at J9.

Two specific AG/SG calibration experiments were performed during the observation period: the first one in September 2016 having a duration of 149 h (6.2 days) and used to calibrate iGrav29, iGrav30, iGrav31, and iOSG23; the second one in July 2017 having a duration of 170 h (7.1 days) and used to calibrate iGrav15, iGrav32.

Note that numerous absolute calibration experiments were done with C026 since 1996 (Amalvict et al., 2001; Calvo et al., 2014; Crossley et al., 2018; Riccardi et al., 2012; Rosat et al., 2009) leading to the very well determined value of $- 792 \pm 1$ nm/s²/volt.

iGrav15 was first calibrated by FG5#206 in J9 and after cold transportation to the Theistareykir geothermal site in Iceland it was calibrated again. The two calibration factors found in J9 and Iceland lead to a nearly identical value $- 935 \pm 6$ nm/s²/V (Schäfer et al., 2020). No absolute calibration could be performed for iGrav6 at J9.

2.2. Relative Calibration

It has been shown in previous studies that the internal SG stability ($\sim 0.1\%$) as derived from tidal analyses is more than ten times better than the stability that can be achieved by calibration repetitions with an absolute gravimeter (Calvo et al., 2014). Besides, absolute gravity measurements are affected by noise which will limit the precision of the retrieved scale factor. Assuming one of the SGs operating in our Observatory possesses an accurate calibration, we can estimate the scale factors of other SGs by minimizing the differences of raw time records that should measure the same changes in gravity being located at the same place (at least inside the same building). We may hence expect to improve the precision on the scale factor estimates. However, we have to state here that a relative calibration can never be more accurate than the calibration of the instrument used for the relative calibration. It can only enhance the precision of calibration but not the accuracy. Using another relative gravimeter to calibrate an SG was already tested by Meurers (2012) and by Riccardi et al. (2012). The latter for instance applied this method to the C026 using the gPhone-54 spring gravimeter data. Precision on the SG scale factor was around 0.01% while using absolute FG5 measurements it was limited to 0.4%.

To obtain the relative scale factors we applied a multi-regression method on the SG raw signal (in volts) with respect to iOSG23 gravity (in nm/s^2) and to time (assuming a linear or second order polynomial drift). In addition, we also computed the scale factor for a moving window (2 days shifted by half a day) both with unfiltered data and filtered data using a band-pass filter centered on the tides, between 0.5 and 2.5 cycle per day (cpd). The results given in Table 2 are the mean values and standard deviation of the histogram of the scale factor estimates. In this way the error estimate is more robust than the formal error coming from the multi-regression on the entire duration.

A duration of one month of 60 s samples was chosen to have enough precision in the adjustment, except for iGrav32(b) and iGrav6 for which only 11 and 23 days of recording at J9 were available, respectively. Since we do not have all the SG meters

running in parallel at the same time we used two different monthly periods: 1–31 May 2017 for iGrav30, iGrav31, iOSG23; 29 July–28 August 2017 for iGrav29, iGrav15, iGrav32(a), and C026 (GGP1 and TIDE), and additionally: 13–23 October 2017 for iGrav32b and 1–23 October 2017 for iGrav6.

Different tests done on time spans of various lengths (from 11 to 31 days) have shown that there is a small variability of the relative scale factor (a few per mil) and correlation coefficient (less than 1‰) with time length. We also checked that the results are unchanged when we consider the time shift that may exist between different gravimeters. For instance, the largest time shift that is largely due to the TIDE filter of C026, which delays its signal 33 s with respect to iOSG23 (see section on time delays), causes a relative calibration change of $10^{-2} \text{ nm/s}^2/\text{V}$ which is negligible in Table 2.

As expected, the errors in relative calibration are much smaller than the errors in absolute calibration, mostly in the range 1×10^{-4} – 8×10^{-4} (dimensionless); all correlation coefficients are very high (at least > 0.999).

It is noticeable that for iGrav6, iGrav15 and iGrav32, the relative scale factors between pairs of instruments did not change after transport from J9 to Iceland, within 0.01% uncertainty (Schäfer et al., 2020).

2.3. Tidal Calibration Using K1 and M2

The aim of our method in this section is to find out whether the ratio of relative calibration versus absolute calibration inferred from the one-month (May 2017) is confirmed by tidal analysis. We used our longest common operation period of nearly 1 year of iGravs 29, 30, 31 and iOSG23 from 04 August 2016 to 19 June 2017 (321 days) to perform a tidal analysis with the help of ET34-ANA-V61A program (Ducarme & Schüller, 2018; Schüller, 2018). To achieve a better determination of the diurnal and semi-diurnal tides we used an identical FIR zero phase high-pass filter (with 0.8 cpd corner frequency), based on Hanning-Window of 3001 min length) for all data sets. We also assume no phase lag

Table 2
Results for the absolute and relative calibrations of different SG meters in J9

SG and filter	Duration	Rel Cal and error (nm/s ² /V)	Abs Cal and error (nm/s ² /V)	Rel Cal–Abs Cal and error (nm/s ² /V)
iOSG23 (reference)		– 451 ± 0	– 451 ± 2	0 ± 2
C026 GGP1	1 month	– 792.2 ± 0.1	– 792 ± 1	0.2 ± 1
No time shift	29/07/17–28/08/17			
C026 GGP1 with 2 s time shift	1 month	– 792.2 ± 0.1	– 792 ± 1	0.2 ± 1
	29/07/17–28/08/17			
C026 TIDE	1 month	– 791.5 ± 0.1	x	x
No time shift	29/07/17–28/08/17			
C026 TIDE with 32 s time shift	1 month	– 791.5 ± 0.1	x	x
	29/07/17–28/08/17			
iGrav6	October 2017	– 914.2 ± 0.2	x	x
iGrav15	1 month	– 932.3 ± 0.1	– 934 ± 3	1.7 ± 3
	29/07/17–28/08/17			
iGrav29	1 month	– 937.8 ± 0.1	– 940 ± 4	2.2 ± 4
	29/07/17–28/08/17			
iGrav29	1 month	– 937.7 ± 0.1	– 940 ± 4	2.3 ± 4
	1–31 May 17			
iGrav30	1 month	– 917.6 ± 0.1	– 918 ± 4	0.3 ± 4
	1–31 May 17			
iGrav31	1 month	– 850.5 ± 0.1	– 853 ± 4	2.5 ± 4
	1–31 May 17			
iGrav32 (a)	1 month	– 897.4 ± 0.7	– 898 ± 3	– 0.6 ± 3
	29/07/17–28/08/17			
iGrav32 (b)	OCT 2017	– 895.9 ± 0.1	x	x
	~ 13 days			

between the different SG and use the absolute calibration factor for each gravimeter.

The results for iGrav29, iGrav30 and iGrav31 compared to iOSG23 are shown in Table 3 and plotted in Fig. 4, where we kept only the large tide K1 in the diurnal band and M2 in the semi-diurnal band. As expected, the tidal analysis confirms the discrepancy between absolute and relative scale factors.

In the last column of Table 3 the formal precision of the tidal ratios is constant for all estimates and very small (1×10^{-5}). However, the differences between K1 and M2 tidal ratios are 5×10^{-5} for iGrav29, 46×10^{-5} for iGrav30, and 9×10^{-5} for iGrav31 that are larger (and more realistic) values than the formal precision for each wave. Figure 4 shows the excellent agreement of the tidal ratio with the relative calibration ratio except for K1 in the iGrav30/iOSG23 comparison; the definite reason for this is unknown but we show later in Sect. 5.1 that the noise

level of iGrav30 is significantly higher at low frequencies than the other iGravs.

2.4. Spectral Analysis of Tidal Residuals

Another way to test the calibration factors is to perform a spectral analysis of the difference between two calibrated time series which may reveal tidal residuals. In the following we consider iGrav29 versus iOSG23. We will assume that iOSG23 is well calibrated and will investigate the difference with iGrav29 by using different relative scale factors for this meter with increments of 0.4 nm/s²/volt ($\approx 0.04\%$ in proportion) compared to 4 nm/s²/volt uncertainty from AG/SG calibration (see Table 3).

The results based on one month (May 2017) 60 s samples of iGrav29 are shown in Fig. 5 for 4 different relative scale factors close to the value -937.8 nm/s²/volt inferred from the one month regression in May 2017 (see Table 3). It is clearly visible that the smallest tidal residuals at 1 and 2 cpd

Table 3

Comparison of ratio of relative calibration versus absolute calibration for iGrav29, iGrav30 and iGrav31 with respect to iOSG23 as inferred from tidal analysis and time regression

SG	REL. CAL (nm/s ² /V)	AG CAL (nm/s ² /V)	AG CAL/REL CAL	Wave: tidal ratio
iGrav29	− 937.8 ± 0.003	− 940 ± 4	1.00235 ± 0.004	K1: 1.00239 ± 0.00001 M2: 1.00244 ± 0.00001
iGrav30	− 917.6 ± 0.006	− 918 ± 4	1.00044 ± 0.004	K1: 1.00003 ± 0.00001 M2: 1.00049 ± 0.00001
iGrav31	− 850.5 ± 0.003	− 853 ± 4	1.00294 ± 0.004	K1: 1.00291 ± 0.00001 M2: 1.00282 ± 0.00001

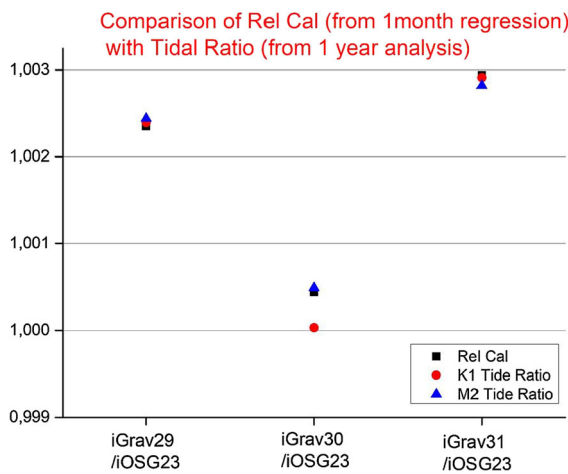


Figure 4

Ratio of relative calibration versus absolute calibration for iGrav29, iGrav30 and iGrav31 with respect to iOSG23 as inferred from tidal analysis (1 year) and time regression (1 month)

appear for this scale factor. If we correct for the 3 s time shift between iGrav29 and iOSG23 (see Table 4) then the tidal residuals in the spectrum of the gravity difference almost vanish (in magenta in Fig. 5). Similarly for iGrav30 and iGrav31 the minimal tidal residuals correspond to the scale factors found from time regression.

It is worth to note that using the absolute calibration factor (− 940 nm/s²/volt) would lead to tidal residuals that are 5–6 times larger when compared to the adjusted relative calibration value as shown on Fig. 6.

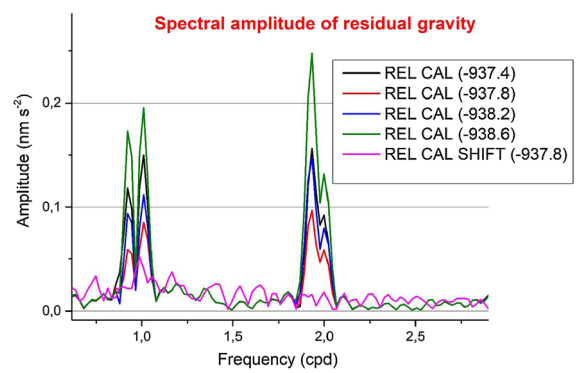


Figure 5

Spectral amplitude of residual gravity between iGrav29 (using different relative scale factors) and iOSG23; frequency units are cycle per day (cpd)

2.5. Time Delay

After having discussed the problem of amplitude calibration, we focus now on the time delays that may exist between the different SGs due to different apparent spring constants (from the magnetic gradient adjustment), masses, damping, filters and electronics. The iOSG23 and the iGravs have a built-in Butterworth filter with corner period of 5 s and a time delay of 1.54 s followed by an anti-aliasing lowpass FIR filter consisting of 69 terms with a time delay of 4.25 s. In addition, there is a timing error of − 0.62 s in the firmware implementing the FIR filter so its delay is reduced to 3.63 s. The SG C026 has a built-in electronic low-pass filter called “GGP1” with a corner period of 16.3 s and a time delay of 8.2 s (Warburton, 1997). A TIDE filter is also integrated to the electronics of the SG C026 with a corner period

Table 4

Time delays (in sec) between different SG using a cross-correlation method based on simultaneous data with various samplings and durations of analysis periods

	Time delay (s) 1 month of 1 s samples low pass filtered	Time delay (s) 1 month of 60 s samples after decimation	Time delay (s) 1 year of 60 s samples
iGrav6/iOSG23 ^a	3	3	X
iGrav15/iOSG23	3	3	X
iGrav29/iOSG23	3	3	2
iGrav30/iOSG23	2	2	3
iGrav31/iOSG23	2	2	1
iGrav32a/iOSG23	1	1	X
iGrav32b/iOSG23 ^b	1	1	X
C026 (GGP1)/iOSG23	3	2	2
C026 (TIDE)/iOSG23	33	32	31
C026(TIDE)/C026(GGP1)	30	30	30

^aOnly ~ 23 days available in October 2017

^bOnly ~ 13 days available in October 2017

of 72 s and a time delay of 32 s (Van Camp et al., 2000).

As before, we will use the one-month time series in May 2017 of iGrav29, iGrav30 and iGrav31 and iOSG23 sampled at 1 s to investigate this point. We also considered the time series of the older compact SG C026 with data low pass filtered by two classical electronic anti-aliasing filters widely used in the past namely GGP1 and TIDE filters. For iGrav32 and iGrav6 all available data in October 2017 were used but one has to keep in mind that the time series are shorter than one month and, even more important,

that these data are fully subject to initial drift (see Sect. 3).

We apply a cross-correlation method between two time series and determine the time of maximum cross-correlation to estimate the time delay between two time series.

If the instrumental response as a function of frequency is identical (except timing error) for two systems, calculating a cross-correlation between their output will give a unique estimate of the difference in timing. In the present context, this is not the case. Then, applying a cross-correlation method will only give an estimate of timing difference averaged over a certain range of frequency. A reasonable result was obtained because the largest signals are the semi-diurnal and diurnal waves with frequency range below $1e-3$ cycle/sec where the phase response is almost flat (inferred from Fig. 7).

As expected, the same cross-correlation analysis done on raw (unfiltered) 1 s samples led to slightly different results (not shown) because of the influence of high frequency content (microseisms, earthquakes) (see Table 4). The values of the time delays do not depend on the sampling (1 s or 1 min) if the high frequency content of the sec samples has been filtered out. The time delays derived from 1-year correlation analysis (August 2016–July 2017) for iGrav29, iGrav30 and iGrav31 are similar to the values inferred from one-month analysis. This analysis

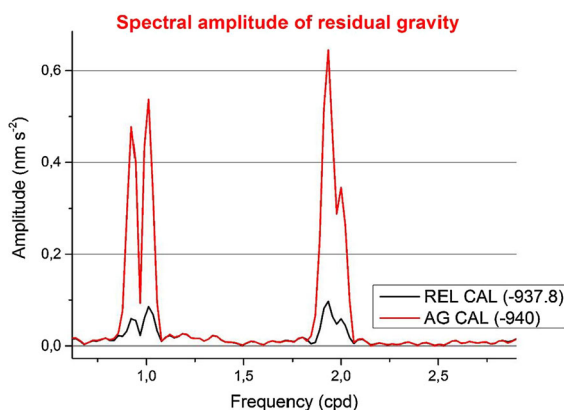


Figure 6

Spectral amplitude of residual gravity between iGrav29 (using best relative and absolute calibration factors) and iOSG23

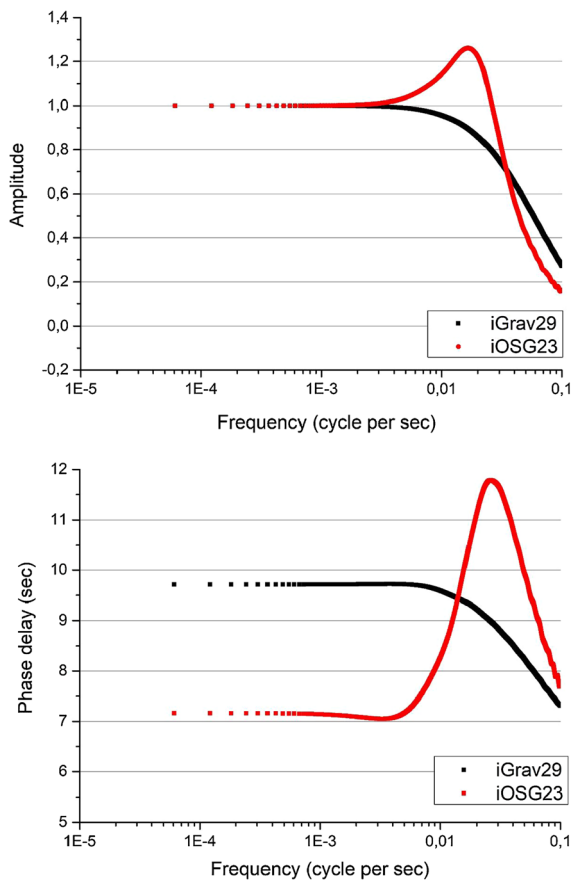


Figure 7

Amplitude and phase transfer function for iGrav29 and iOSG23

implies time invariance of the filter time delays. We also checked that the time delay combinations between channels obey the transitivity rule where $\text{cor}(A/C) = \text{cor}(A/B) + \text{cor}(B/C)$, as can be seen in Table 4 for the filtered data TIDE and GGP1 implemented on C026.

A phase experiment test using the method outlined in Van Camp et al. (2000) where injecting known voltages (usually a sinusoidal or step-like functions) into the control electronics of the system enables one to determine time delay with a precision of better than 0.1 s, was done on iGrav29 and iOSG23 to retrieve the full transfer function both in amplitude and phase delay of these two instruments. The time delay becomes constant for frequencies below 10^{-3} cpd (Fig. 7). The phase delay of iGrav29 with respect to iOSG23 is found to be $9.71 \text{ s} - 7.16 \text{ s} = 2.55 \text{ s}$. Since these two SGs have

identical electronics, this phase difference must be caused by the different masses of the spheres, the force gradient and damping in these instruments. As done before for the amplitudes, we also use the tidal analysis of 1 year of data to check the respective time delays by computing the M2 and K1 phase lags. The 2.55 s phase delay between iGrav29 and iOSG23 is in close agreement with the tidal results (see Fig. 8).

A similar experiment that used injected sine waves rather than a step function was done on C026 in 2012 and led to a time delay of $9.7 \pm 0.4 \text{ s}$ from the GGP1 filtered data.

If we assume the time delay of iOSG23 is 7.16 s, the experimental phase delay of C026 with respect to iOSG23 would be 2.54 s. This value is very close to the ones plotted in Fig. 9.

3. General Initialization Procedures for SGs

Over many years a general procedure has been developed to minimize drift and offsets in SGs. Figure 7 of Hinderer et al. (2015) shows a diagram of the SG sensor and its major components. The main superconducting components are the sphere, the magnet coils, the heat switches and the superconducting shield. The sphere position is sensed by the linear transducer consisting of the upper, central and lower capacitance plates. All of these components are

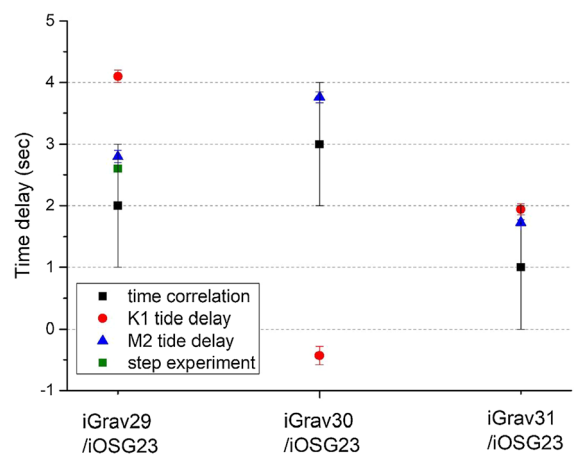


Figure 8

Comparison of time delays for iGrav29, iGrav30 and iGrav31 with respect to iOSG23, using time correlation or tidal analysis of major waves K1 and M2

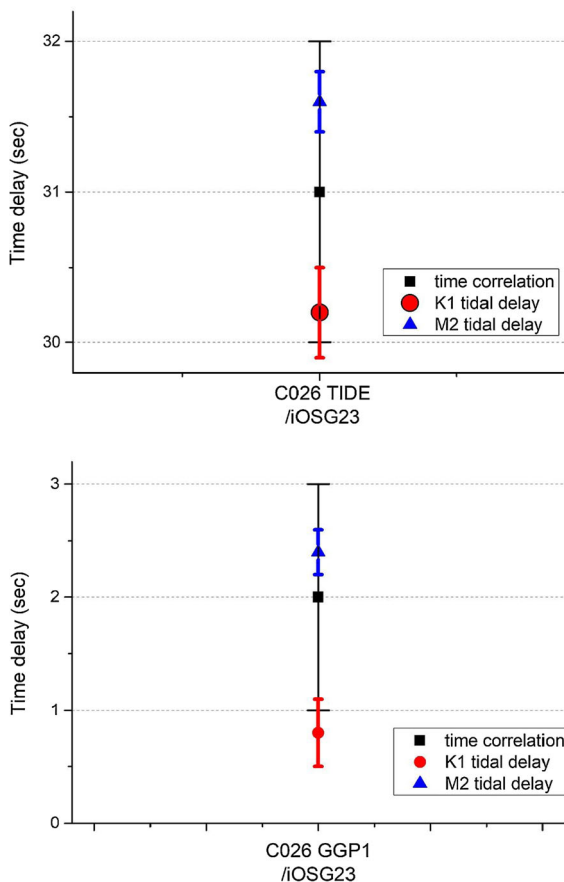


Figure 9

Comparison of time delays for C026 (TIDE filter) with respect to iOSG23, using time correlation or tidal analysis of major waves K1 and M2 (top); comparison of time delays for C026 (filter GGP1) with respect to iOSG23, using time correlation or tidal analysis of major waves K1 and M2 (bottom)

mounted on or inside the Al or Cu body of the sensor which is positioned inside a vacuum can that is surrounded by a liquid helium bath at 4.2 K. The body is suspended from the lid of the vacuum can with three G-10 fiberglass laminate posts that thermally isolate the body from the helium bath. With this isolation, a Germanium thermometer operating in a Wheatstone bridge with a temperature control heater precisely controls the temperature of the body at about 4.4 K or 0.2 K above the bath temperature. In addition, there are several components used only during the installation of the sensor: a Body heater and a Si diode thermometer reside on the top of the magnet form and are used to heat the magnet form (Body) and record its temperature (Body-T); a Mu metal shield

surrounds the vacuum in order to reduce the Earth's magnetic field; and a charcoal getter to add and to extract gas from the vacuum can. The charcoal getter consists of a small Cu or Al cylinder that contains charcoal pellets glued to a heater. The getter cylinder can either be outside the vacuum can and connected by a tube as shown in the diagram or it can be inside the vacuum can. When the charcoal is at cryogenic temperatures it adsorbs He gas from the vacuum can. This gas can be released by activating the getter heater to heat the charcoal above 70 K.

After cooling the Dewar and gravity meter sensor to 4.2 K, initialization of SGs generally includes five standard procedures that are followed in a well determined order. First, a body heater is used to heat the sensor body and all the superconducting components inside the vacuum can above 32 K which is well above the superconducting transition temperature of Nb and the mu-metal shield is demagnetized. This minimizes the presence of the Earth's magnetic field trapped in the sphere and coils before levitation. Second, the sensor body is fast cooled to 4.2 K by briefly heating the charcoal getter. This releases He gas into the vacuum container which conducts heat directly between the body and the walls of the vacuum can. This cools the body in a few minutes versus the 10 to 12 h if cooling were only via the G-10 posts. After cooling to 4.2 K, the temperature control is turned on which raises the temperature to the control point near to 4.4 K. Third, the sphere is levitated, and the magnetic gradient adjusted. Fourth, the sensor is low temperature annealed by raising the temperature to about 5.2 K and lowered back to 4.2 K. This reduces the magnitude of offsets induced during excursions of the temperature control between 4.2 to 5.2 K. Then the temperature control is turned on again and the sensor returns to its control point near to 4.4 K. And fifth, the thermal levelers are used to tilt-desensitize the sensor.

Variations to the installation may occur: some iGravs have side coils and the field is trapped after the demagnetization but before the fast cooling; He gas may or may not be released from the getter to cool from 5.2 K during the low temperature annealing; and the order of low temperature annealing and tilting may be interchanged. In addition, some variations may occur due to operator error during set-up

and initialization at a new site when site preparation is not complete or other difficulties occur. For example, during the July 2016 initialization at J9, two errors occurred. For iGrav29, the low temperature annealing was done improperly. The sensor was heated to 5.2 K, but it was then cooled back to its control point at 4.4 K rather than being cooled fully to 4.2 K before being returned to the control point while, for iGrav30, the low temperature annealing was omitted entirely.

4. Instrumental Drift

In this section we investigate the instrumental drift of the iGravs and iOSG23 collocated at J9. Previous studies have reported that the instrumental drift of SGs can be modelled by a short-term exponential function followed by a linear trend of 10 to 50 nm/s²/year (Crossley et al., 2004; Hinderer et al., 2015; Van Camp & Francis, 2007). However, for records longer than 10 years, Van Camp and Francis (2007) showed that the long-term drift for GWR C021 is better modelled by an exponential. More recent work by Schäfer et al. (2020) showed that the initial drifts in GWR iGrav SGs require additional short-term exponential functions to model rapid drifts that occur immediately after initialization and sphere levitation. In addition, Dykowski et al. (2019) have shown for iGrav27 that drifts also occur in the body temperature (Body-T) that are highly correlated (0.98) with the gravity drifts and that these can also be modelled by an initial exponential term followed by a linear drift.

In this work, we model the instrumental drift of SG as the sum of several exponential decaying functions (up to 3) and a linear term that remains very stable in time after the exponential terms become negligible.

The model of instrumental drift is hence as follows:

$$g(t) = g_0 + A_1 e^{-\frac{t-t_0}{\tau_1}} + A_2 e^{-\frac{t-t_0}{\tau_2}} + A_3 e^{-\frac{t-t_0}{\tau_3}} + C(t - t_0) \quad (1)$$

where $g(t)$ is the gravity as a function of time t , with initial values g_0 and t_0 , A_1 , A_2 and A_3 the amplitudes,

τ_1 , τ_2 and τ_3 the time constants, and C the coefficient of the linear term. A Levenberg–Marquardt iteration algorithm is applied to reach convergence in the fit. The functional drift of the Body-T can also be approximated by exponential terms plus a linear term very similarly to what we do for the gravity signal. Long term changes in the Body-T sensor indicate that thermal gradients continue to change in the sensor over long periods of time. It is hypothesized that this is from the charcoal getter continuing to adsorb He gas out of the vacuum can and that this is one source of drift.

We first investigate the long-term behavior of iOSG23 which was installed in February 2016 and still operates today. This meter will act as reference gravimeter throughout this study. We use a series of 16 AG measurements taken at J9 with FG5#206 during the years 2016–2019 to infer the iOSG23 drift components. In another section we examine the initial drift and Body-T behavior of 3 iGravs (#29, #30 and #31) that were all initialized in June 2016 and re-initialized in October 2016. Also, since iGrav29 was re-levitated both in November 2020 and December 2020, we can investigate how the initial gravimeter drift and Body-T drift evolve during these additional re-levitations.

4.1. Long Term Drift of iOSG23

We investigate the drift behavior of iOSG23 using a 4.1 year-long record (1520 days from February 3, 2016 to April 20, 2020). To prepare the data, a first decimation filter is used from 1 to 60 s. The major gravity steps in iOSG23 are removed by comparison to a data record prepared in the same way for iGrav29 which was operating nearby at J9. Subsequently, spikes and large earthquakes are removed by interpolating over the disturbances. After all corrections are made a second decimation filter reduces the data to hourly intervals.

In the following we determine the long-term linear drift by fitting AG data to the last 3 years of iOSG23 data. In this case we are not considering the exponential drift that typically occurs immediately after the initialization of the gravimeter. Then, after removing this linear drift from the entire data set, we

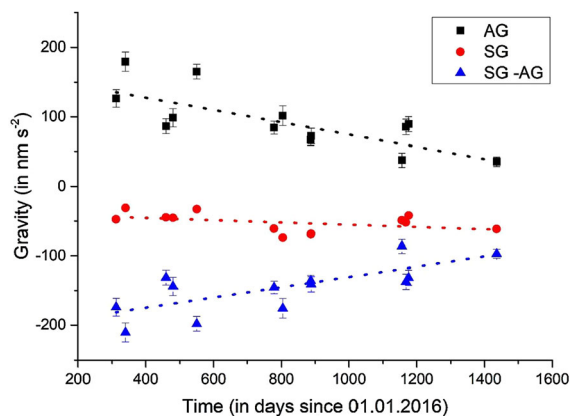


Figure 10

Determination of iOSG23 instrumental linear drift rate using AG (FG5#206) values

use a non-linear curve fitting tool based on several exponentials.

Before applying this procedure, we first need to compare the iOSG23 residual values (observations corrected for the local tide, barometric pressure and polar motion) to measured AG values at J9 using FG5#206 over the same period (corrected exactly in the same way).

In Fig. 10, the black squares show the values of the AG measurements minus the mean value of the AG measurements taken in the period from 3 October 2016 to 12 June 2019, which covers the record of iOSG23 data. These values are offset by 100 nm/s² so that the 3 plots of the AG (black squares) values, the SG (red dots) values and the difference SG-AG (blue triangles) values do not overlap and provide an easier visual inspection.

In the determination of the SG linear drift, we excluded the first 3 points in 2016 which are likely to be affected by getter pump out and are part of the initial exponential drift term.

The results of the linear fitting procedure of the data sets shown in Fig. 10 are given in Table 5.

Table 5

Drift rates: results of the linear fit to AG (FG5#206) and SG (iOSG23) data

	Linear trend and error (nm/s ² /year)
AG (FG5#206)	-32.3 ± 7.5
SG (iOSG23)	-6.0 ± 5.1
SG-AG	27.0 ± 6.3

For the AG points, we measure a decrease in gravity of $-32.3 \text{ nm/s}^2/\text{year}$ with $R^2 = 0.59$ most probably of hydrological origin since vertical motions due to tectonics are too small as inferred from GPS measurements at J9. For the iOSG23 data we measure a smaller decreasing rate of $-6 \text{ nm/s}^2/\text{year}$ with $R^2 = 0.11$ and for the difference SG-AG, we get a positive rate of $+27.0 \text{ nm/s}^2/\text{year}$ with $R^2 = 0.59$.

This result indicates that the instrumental linear drift determined for iOSG23 by comparison to the AG measurements is $+27.0 \text{ nm/s}^2/\text{year}$ which is a typical value for other SGs. However, there is a high relative uncertainty (23.3%) for this drift rate. The dispersion of the points in Fig. 10 that are not perfectly aligned on a straight line is not clear. It is possible that the AG errors are underestimated or that the AG senses slightly different hydrological effects due to its placement in the vault.

After removing the drift inferred from the AG points, the iOSG23 residual gravity data have been fitted to a combination of exponential and linear terms according to Eq. (1). The fit results are given in Table 6 and Fig. 11 shows the superposition of the fitted model to the iOSG23 gravity data.

The fitted iOSG23 instrumental linear drift rate of $24.4 \text{ nm/s}^2/\text{year}$ is close to the value of $27.0 \text{ nm/s}^2/\text{year}$ in Table 5 but differs because the fitting procedure uses all the hourly data from iOSG23 in one case and only the few episodic AG/SG parallel measurements on the other case.

After removing a linear term of 0.3 mK/year , a similar method is used to fit to the Body-T data for iOSG23. The Body-T time constants are shown in Table 6 and a comparison of the data and the fit curve are shown in Fig. 12. Two of the time constants for gravity and Body-T are similar with a very short time delay t_1 less than half a day and a very long one t_3 close to 150 days. The fitting process for the Body-T converges to find the intermediate terms ($A_2 = -0.3 \text{ mK}$, $t_2 = 57.2 \text{ days}$) but does not converge to find similar intermediate terms for the gravity residual signal.

The correlation we already introduced between gravity and body temperature drifts appears very clearly on Fig. 13. The left part is coming from the strong exponential initial drift occurring on both signals. Later during instrument operation, gravity

Table 6

Results for the exponential and linear fitting of iOSG23 gravity and Body Temp signal; symbols in the header are the same as in Eq. (1)

Data starts 03/02/2016	A_1	t_1	A_2	t_2	A_3	t_3	C
Record length 1520 days							
iOSG23 gravity	nm/s ²	days	nm/s ²	days	nm/s ²	days	nm/s ² /year
3 exp fit	- 131.2	0.4	x	x	- 144.4	153.5	24.4
iOSG23 Body Temp	mK	days	mK	days	mK	days	mK/year
3 exp fit	- 1.8	0.4	- 0.3	57.2	- 0.4	143.2	0.3

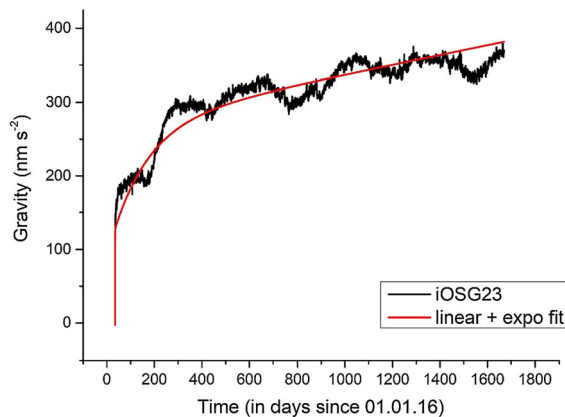


Figure 11

Gravity residual signal of iOSG23 as a function of time; the observations are in black and the best fit combining exponential and linear terms according to Table 6 are in red

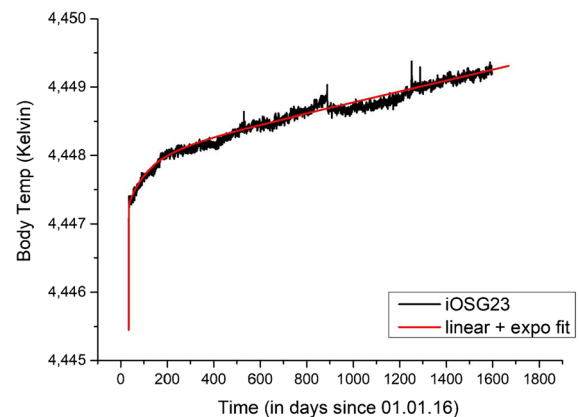


Figure 12

Body-T signal of iOSG23 as a function of time; the observations are in black and the best fit combining exponential and linear terms according to Table 6 in red

and Body-T are still correlated but the correlation is noisier.

As observed by Dykowski et al. (2019), the instrumental drift highly correlates with Body Temp. This is true for the exponential part after levitation as well as for the long-term linear part. The correlation factor between gravity and Body-T signals for iOSG23 is rather large (0.88). This suggests that the long-term linear drift (or part of it) in SGs might in fact be due to this continued adsorbing process of the getter.

4.2. Drift Behavior of iGravs

4.2.1 Overview of Data

iGrav29, iGrav30 and iGrav31 were first initialized in July 2016 at J9. Since there were many disturbances during and after this installation, it was decided to

repeat the entire initialization process on iGrav29 and iGrav30 in October 2016; while only low-temperature annealing of iGrav31 was done to complete its previous initialization. iGrav #30 and #31 then operated at J9 until the end of June 2017 at which time iGrav30 was shipped cold for installation at the Strengbach catchment in the French Vosges mountains (Chaffaut et al., 2020) while iGrav31 was warmed to room temperature for its future shipment in late March 2019 to a mountain site directly above GWR iOSG24 which is operating in the LSBB underground laboratory in Rustrel. iGrav29 was also scheduled to move to another water catchment of the Ozcar network (Gaillardet et al., 2018) but, due to COVID-19 restrictions, it continues to operate at J9 presently. For reasons discussed below, it was warmed to room temperature in October 2019 and reinitialized for a 3rd time. In December 2020 an experiment was done where—without activating the

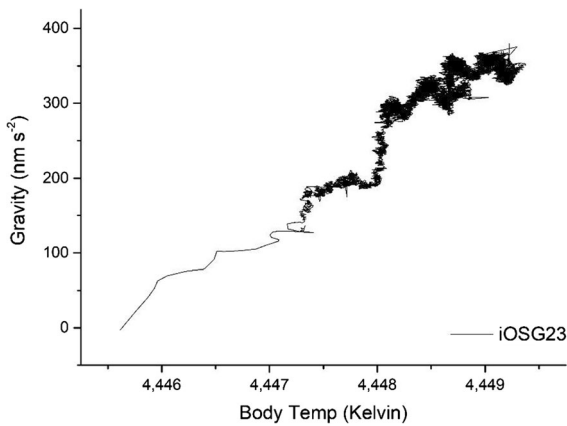


Figure 13

Correlation between iOSG23 gravity residuals and body temperature signals using the 4.2-year data set

getter—the sphere was lowered, and the magnets purged of currents. Then after a few days the sphere was again re-levitated without using the getter.

In analyzing data from these iGravs, we used iOSG23 as a reference instrument so that we could look directly at the difference signals iGrav29–iOSG23, iGrav30–iOSG23 and iGrav31–iOSG23. It is a major advantage to use iOSG23 as a reference rather than a calculated tide model because iOSG23 provides a precise measure of all gravity changes while any model is incomplete: the model does not include hydrological signals, it assumes a constant admittance to the atmosphere, and it approximates many of the long-period tidal signals. We first correct the iOSG23 data for the linear and exponential drifts previously found (see Table 6). Then the gravity differences are taken between the three iGravs and the corrected iOSG23 signal using the calibration factors listed in Table 2. Earthquakes, offsets and other disturbances are removed, and the data are further filtered and decimated to hourly intervals.

The results for the initial drifts of iGrav29–iOSG23, iGrav30–iOSG23 and iGrav31–iOSG23 are plotted in Fig. 14 (where arrows show the initialization events) along with the residual gravity signal for iOSG23 calculated with a tidal model and corrected for its exponential and linear drifts from Table 6. Long-period tides, polar motion and hydrology are not corrected for, so they appear clearly on the iOSG23 residual signal but they do not appear on the difference signals. The difference drift curves are

very smooth since all the unmodelled signals that show up in the iOSG23 curve are eliminated in the iGrav29, iGrav30 and iGrav31 difference curves. It is not possible to measure such drifts with this high precision without using a reference SG. Figure 15 shows the Body temperature data over the same time period as shown for the gravity data in Fig. 14.

There are several features on these data that stand out. In Fig. 14, a negative drift is observed immediately after the first initialization of iGrav29 in July 2016 (red line). After the second initialization in October 2016, the residual drift for iGrav29 looks reasonable at first, but after about 180 days it turns into a negative drift rate of about $-51.9 \text{ nm/s}^2/\text{year}$ which was observed for the next 2 years (green line). We also observe increasing noise levels in both iGrav29 and iOSG23 at the start of this negative drift period. This is likely from build-up of ice in neck of iGrav29. In contrast to Fig. 14, all the Body-T drifts in Fig. 15 are smooth curves in the positive direction. The only uncertainty in the Body-T data is the offset that occurs in the iGrav29 Body-T after the October 2019 re-initialization. This is most likely a problem with the thermometry circuitry measuring the Body-T but this remains unproven.

We separate the data into three sections to model the drift curve function according to Eq. 1 and to examine the correlation between the gravity residual and Body-T. The present section includes the July

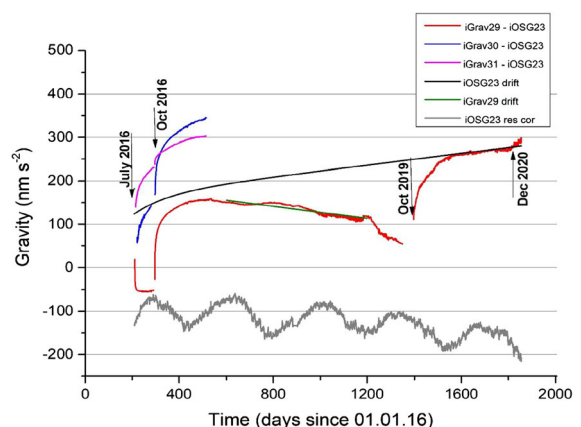


Figure 14

Gravity difference signals between iGrav29, iGrav30 and iGrav31 and iOSG23 corrected for its drift curve for the entire 4.5 year-long record at J9, Strasbourg

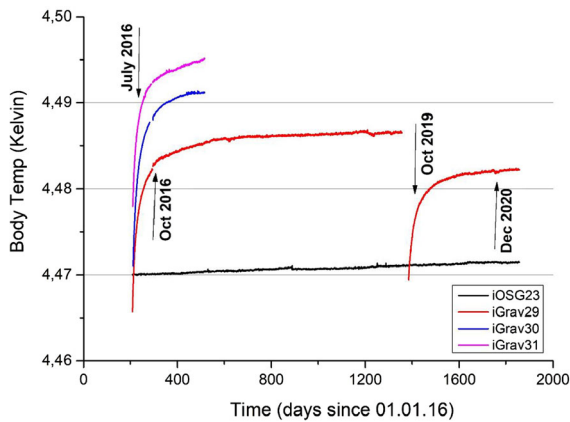


Figure 15

Body temperature signals for iGrav29, iGrav30 and iGrav31 and for iOSG23 for 4.5 year-long record at J9, Strasbourg

and October 2016 initializations, the next section examines the initialization in October 2019, and the third the re-levitation in December 2020.

4.2.2 July and October 2016

Figure 16 shows the data from July 28, 2016 to March 5, 2017 in more detail. These data include two specific time spans: a first one that lasted about 75 days after the installations on July 28, 2016; a second one that lasted 219 days after the re-initializations of iGrav29 and iGrav30 and the low temperature annealing of iGrav31 (that occurred on October 23, 2016). The data for iGrav31–iOSG23 are the same as in Fig. 14. However, before fitting the data for iGrav29–iOSG23 to Eq. 1, they must be corrected for its negative drift. Otherwise, the negative drift will interfere with the fitting parameters for the longer-term exponential functions. A decision was also made to correct iGrav30–iOSG23 for the same negative drift since it appears that the iGrav30–iOSG23 data was also beginning to trend negative in Fig. 16. With these corrections made, the drift curves for all 3 iGravs are similar for the last 100 to 150 days of Fig. 16.

There is a striking difference between the gravity difference data of Fig. 16 and the Body-T data of Fig. 17 in that the Body-T curves behave continuously across the October 2016 re-levitation while there is a discontinuity in the gravity differences after the October 2016 levitation in terms of generation of

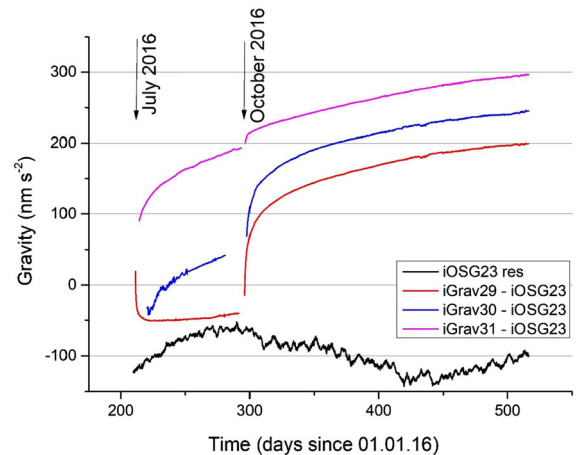


Figure 16

Initial drift curves of gravity differences iGrav29–iOSG23, iGrav30–iOSG23, iGrav31–iOSG23 and iOSG23 residual signal after initialization in July and October 2016 through to March 5, 2017 and after correcting iGrav29–iOSG23 and iGrav30–iOSG23 for the negative drift observed in Fig. 14

a new initial drift. This is slightly misleading since rapid drifts do occur in the Body-T data immediately after the initialization procedures, for example for iGrav29 Body-T rapid drifts of about 50 to 70 mK occur at the beginning of both the July and October installations; however, since they last less than 1 h, they are removed by the filtering and decimation process. Corresponding drifts occur in the gravity differences, but these are difficult to observe since they occur during the initialization procedures. Nonetheless, the long-term Body-T rapidly returns to its previous functional form as displayed in Fig. 17.

The continuity of the Body-T data shows that the gas released from the getter and the distribution of gas in the vacuum can may depend upon the history of its use. He gas could be bound more tightly to the getter material after it has remained cold for a long time so that less gas is released when it is heated. Also, there are different time constants associated with gas pumped out of or reentering different locations inside the gravity sensor. For example, short time constants for the open volume inside the vacuum can, intermediate time constants for gas located between the shield and vacuum can, and long-time constants for gas trapped inside the magnet coils.

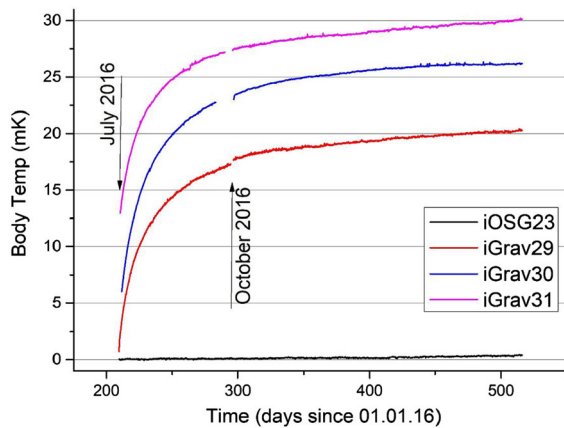


Figure 17

Initial drift curves of Body temperatures for iGrav29, iGrav30 and iGrav31 after the initializations in July and October 2016 through to March 5, 2017

In Table 7, we show the fit coefficients of two exponential functions to both the gravity difference and Body-T data shown in Figs. 16 and 17; the used formalism is the same as in Eq. (1), but neglecting the third exponential ($A_3 = 0$). For the Body-T data, we fit a linear drift to the last 60 days data and subtracted it before fitting with two exponential

functions. We see remarkably similar functions for iGrav29, iGrav30 and iGrav31 Body-T exponentials with: A_1 varying between -6 to -9 mK; t_1 between 8 to 12 days; A_2 between -8 to -10 mK; t_2 between 40 to 60 days; while the linear terms vary more widely between 0.5 to 2.7 mK/year.

A similar fitting procedure was done for the Gravity difference data starting October 2016. In this case, the fitting functions for iGrav29–iOSG23 and iGrav30–iOSG23 were very close: with A_1 between -56 and -74 nm/s²; t_1 between 3.2 and 3.7 days; A_2 between -70 to -74 nm/s²; t_2 between 44 and 51 days; and linear terms both close to 71 nm/s²/year. The amplitudes for the iGrav31–iOSG23 days are smaller ($A_1 = -12$ and $A_2 = -41$ nm/s²) while t_1 is shorter (1.4 days) and t_2 longer (84.9 days) with a steeper linear fit of 77 nm/s²/year. It is not surprising that these amplitudes (seen both in Table 7 and Fig. 16) are much smaller for iGrav31 than for iGravs 29 and 30. The iGravs 29 and 30 were completely re-initialized (sphere lowered and magnet currents purged, bodies heated to 32 K and fast cooled to 4.2 K by adding gas from the getter, spheres re-activated, bodies low temperature annealed,

Table 7

Amplitude and time constants of the exponential fitting of iGrav29–iOSG23, iGrav30–iOSG23 and iGrav31–iOSG23 gravity signal for 72 days after July 2016 levitation and 219 days after October 2016 levitation and for iGravs 29, 30 and 31 body temperatures after July 2016 initialization (291 days)

Gravity differences	A_1 nm/s ²	t_1 days	A_2 nm/s ²	t_2 days	C nm/s ² /year
July 2016 (72 days) data					
iGrav29–iOSG23 ^a	44.4	0.6	18.1	8.2	N/A
iGrav30–iOSG23	– 33.3	7.1	– 104.8	154.3	N/A
iGrav31–iOSG23 ^b	– 31.7	7.4	– 78.7	71.6	N/A
October 2016 (219 days)					
iGrav29–iOSG23	– 74.1	3.2	– 74.4	50.8	70.8
iGrav30–iOSG23	– 55.6	3.7	– 70.1	43.7	71.1
iGrav31–iOSG23 ^c	– 12.2	1.4	– 41.4	84.9	77.2
Body temperatures	A_1 mK	t_1 days	A_2 mK	t_2 days	Linear mK/year
July and October 2016 (291 days)					
iGrav29 Body-T	– 6.0	8.1	– 10.0	40.1	2.3
iGrav30 Body-T	– 9.0	12.6	– 10.0	61.3	0.5
iGrav31 Body-T	– 6.0	10.1	– 8.0	40.2	2.7

^aLow temp. annealing done improperly

^bNo low temp. annealing done

^cLow TEMP. annealed only

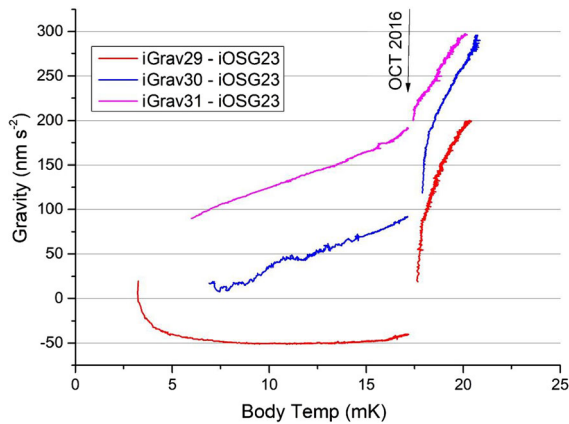


Figure 18

Correlation between iGrav-iOSG23 difference signals and Body Temperatures for iGrav29, iGrav30 and iGrav31 for both the July and October 2016 initializations

and sphere recentered). In contrast iGrav31's body was simply low temperature annealed and then the sphere recentered.

We have also fit 2 exponential functions to the gravity differences following the July 2016 initialization. In these cases, due to the shorter records, we chose to fit 2 exponential terms without first subtracting a linear term. In spite of the shorter records, the different analysis techniques and the quality of the data, the fits for iGrav30-iOSG23 and iGrav31-iOSG23 are still similar to the October 2016 fits although both the t_1 and t_2 time constants are longer. In contrast, the fit of iGrav29-iOSG23 is clearly anomalous with positive amplitudes for both A_1 and A_2 . This is most certainly due to the incomplete low temperature anneal procedure done for iGrav29 in July 2016.

An alternative method to determine the relationship between the gravity difference signals and the

Body temperatures is to measure the correlation between these two data sets directly. Strictly speaking the iGrav-iOSG23 gravity differences should obey a function of the iGrav-iOSG23 Body-Temp differences but since the Body-Temp changes for iOSG23 are so small (see Fig. 12) compared to the iGrav changes we have neglected them. The results of this analysis are shown in Fig. 18 for both the July and October 2016 initializations and shows a more complicated relationship between the initial drift and the Body-T than the nearly linear relationship that was observed in Fig. 13.

For the sake of completeness, we have also indicated in Table 8 the initial drift values we found for iGrav6, iGrav32a and iGrav32b (before and after upgrade at GWR respectively) and iGrav15 which were installed in summer and fall 2017. Notice that some of the fits are done on very short records because of the short availability at J9 (especially iGrav32a and iGrav32b). We do not discuss here the impact of transportation in cold state (or warmed up) on the initial drift rates of SGs. Such a discussion for iGrav6, 15 and 32 after transportation from J9 to Iceland is done in Schäfer et al. (2020).

In Table 8 the short time constant t_1 is close to 0.4 day and t_2 in the range 1.7–3.3 days. In terms of amplitude, the largest one is for iGrav6 (both for A_1 and A_2). Because of the short available durations only short-term exponential terms can be estimated and the long-term drift behavior remains unknown.

4.2.3 October 2019

In October 2019 we decided to re-initialize iGrav29 for a 3rd time. The reason was to confirm the premise (Schäfer et al., 2020) that iGravs with negative drifts

Table 8

Amplitude and time constants of the initial exponential fitting of iGrav6, iGrav32a, iGrav32b, iGrav15 gravity signal using two exponentials (A_1 , t_1 , A_2 , t_2)

2 exponential fit after linear term removed	A_1 (nm/s ²)	t_1 (days)	A_2 (nm/s ²)	t_2 (days)
iGrav6-iOSG23 (25.1 days)	- 39.3	0.4	- 67.8	3.3
iGrav32a-iOSG23 (15.8 days)	- 10.4	0.4	- 40.9	2.1
iGrav32b-iOSG23 (10.4 days)	- 4.4	0.3	- 24.6	2.0
iGrav15-iOSG23 (18.3 days)	- 4.1	0.3	- 33.3	1.7

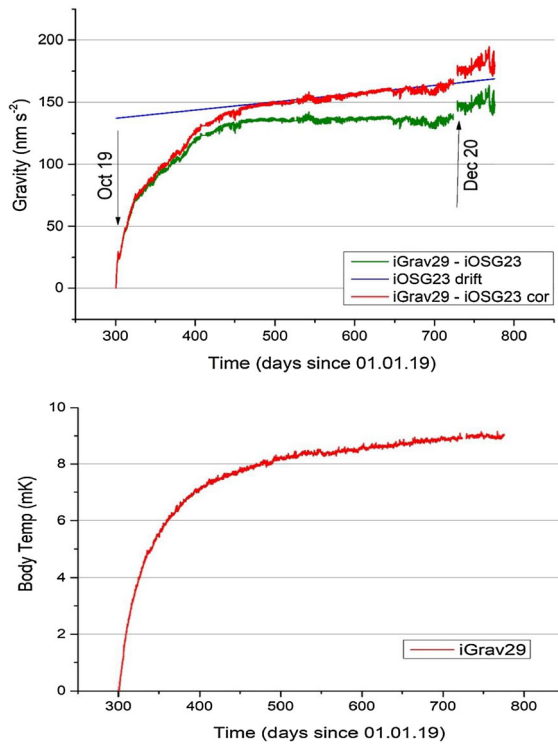


Figure 19

Gravity difference iGrav29–iOSG23 (top) and Body-T (bottom) for October 2019 re-initialization and December 2020 re-levitation

could be restored to normal operation by warming them to room temperature and re-initializing them. In addition, it was recommended not to trap flux with the side coils if there were plans to move an iGrav in the future. Therefore on September 12, 2019, the refrigeration system was turned off and the liquid He evaporated in about 10 days. On October 1, the Dewar was pumped out for 48 h with a primary and

turbomolecular pump to reduce its pressure from 56 to 5.6 Pascal; and on October 3, the refrigeration system was turned back on. Cooling and refill with liquid He took an additional 22 days, so the re-initialization took place on October 26, 2019. In this case, all the initialization steps were rigorously followed, and no flux was trapped in the side coils.

Figure 19 shows the drift analysis of 423 days following the October 2019 initialization. The green trace in the top panel is the direct difference signal iGrav29–iOSG23 while the lower panel shows the Body-T. Since the green curve becomes flat, it means the drift rate of iGrav29 is nearly identical to that of iOSG23. The red curve is the difference curve with the drift correction made to iOSG23, while the blue line is the calculated drift of iOSG23. This important result confirms that the negative drift in iGrav29 had been eliminated by warming it to room temperature and re-cooling and re-initializing it without trapped flux.

Table 9 shows the fitting parameters for the gravity difference and the Body-T, while Fig. 20 compares the correlation between iGrav29–iOSG23 difference and Body-T for October 2019 with the correlations between iGrav–iOSG23 differences and Body-T for iGrav29, iGrav30 and iGrav31 for October 2016.

From these data and from earlier data (Figs. 18, 13), there is clearly a linear relationship between gravity drift and Body-T as the second exponential fits (A_2 and t_2) become dominant (after 2–3 months). There may also be a linear relationship immediately after the initialization (for the first 2 months) but it

Table 9

Amplitude and time constants of the exponential fitting of iGrav29–iOSG23 and Body-T for 423 days after October 2019 levitation; symbols in the header are the same as in Eq. (1)

Gravity differences	A_1 nm/s ²	t_1 days	A_2 nm/s ²	t_2 days	C nm/s ² /year
October 2019 (423 days) iGrav29- iOSG23	– 22.9	4.9	– 113	62.9	18
Body temperatures	A_1 mK	t_1 days	A_2 mK	t_2 days	Linear mK/year
October 2019 (423 days) iGrav29 Body-T	– 3.3	17.1	– 4.8	73.8	0.68

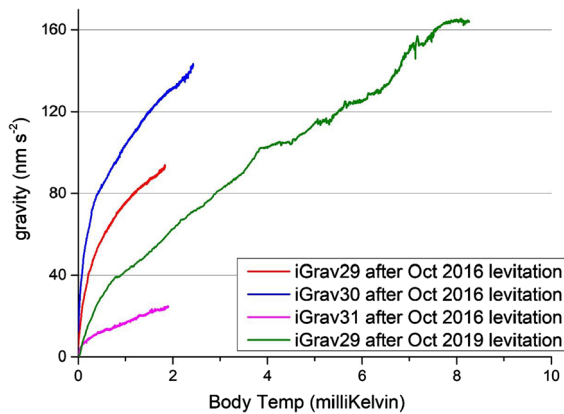


Figure 20

Gravity differences (iGrav-iOSG23) versus Body Temp signals for iGrav29, iGrav30 and iGrav31 after October 2016 levitation (and October 2019 for iGrav29)

clearly is with a different slope after 2–3 months. We note, however, that a linear slope on the Gravity-Body-T plot means that both Gravity and Body-T have the same functional form, not that they are both linear. So, a likely interpretation is that both gravity drift and Body-T have nearly identical exponential functions early after the initialization (first 2 months) and a combination of different exponential and linear functions after 2–3 months. After 2 months a curvature is seen in the correlation plot (Fig. 18) which indicates that the gravity drift and Body-T drift functions are not identical. This is also seen by the fact that the t_1 time constants of the Body-T data are generally longer than that of the gravity drift functions.

4.2.4 December 2020

As a final experiment, on December 26, 2020, the sphere was carefully lowered and the magnet coils purged of currents without activating the getter, so that no additional He gas was released. Then after 2 days, the sphere was re-levitated, a low temperature annealing performed, and the tilt rechecked. Most importantly, the low temperature annealing was performed without using the getter. As we see from Fig. 19, there is no observable change in drift in either the Body-T or the gravity difference signals. While this test positively confirms that initial drifts in iGravs are due to the getter adsorbing gas out of the

vacuum can, it cannot establish with certainty that remaining linear drifts (10–50 nm/s²/year) are caused by continued gas removal or if there is some additional drift mechanism.

4.2.5 Moving SGs

From the data in Schäfer et al. (2020) and the data of this study, we can recommend preferable methods for moving SGs.

1. As a rule, it is always safest to move an SG warm and at room temperature and to re-evacuate the dewar before cooling it at a new site.
2. Any iGrav that uses trapped flux should be warmed to room temperature before it is moved. As discussed in Schäfer et al. (2020), shipping cold iGravs with flux trapping coils activated has produced large negative drifts.
3. Some users may want to move their SG cold at 4.2 K and with the dewar filled with liquid He. First, this eliminates the requirement to cool and fill the dewar with liquid He at a remote site which takes about 10 days. Second—in both cases (1) and (2) above—the initial drift curve will return at the new site and more frequent AG measurements will be necessary to determine the drift curve. In this case, the user can lower the sphere and carefully purge the coils of superconducting currents before moving the instrument, then re-levitate and low temperature anneal at the new site. If this is done carefully—without using the getter to release He gas—either when lowering the sphere or re-levitating the sphere at the new site, it will eliminate the repetition of the initial drift curve of the iGrav at the new location.

5. Environmental and Instrumental Noise Levels

5.1. Observed Noise Levels

In order to have a complete comparison of the SG recording at J9 during a certain amount of time (from a few weeks to several years), we applied a standardized procedure to estimate a noise level that was statistically significant, knowing that these

instruments did not always record simultaneously. We focus here on the SGs but include some other instruments. These are the absolute gravimeter FG5#206 of Micro-g LaCoste, the three spring gravimeters (LaCoste & Romberg Earth Tide gravimeter ET-11, Micro-g LaCoste gPhone-54, LaCoste-Romberg Graviton-EG1194) and the long period seismometers STS-2 which were also operated in J9 in parallel to the SG C026 and analyzed in Riccardi et al. (2011), Arnos et al. (2014), Rosat et al. (2015) and Rosat and Hinderer (2018).

Similar to the procedure by Berger et al. (2004) for stations of the global seismographic network (GSN), we computed power spectral densities (PSDs) of calibrated raw data (1 s sampling) using a modified Welch periodogram (Welch 1967) method applied on 12 h time windows overlapped by 6 h. From the density distribution of PSDs, we computed the 1st, 5th, 25th and 50th percentiles but we have selected only the 5th-tile for the plots in Figs. 21 and 22 to be compared with the GSN noise models of Berger et al. (2004). The new low noise model (NLNM) of Peterson (1993) and the more recent statistical low noise model (SLNM) by Castellaro and Mulargia (2012) are also plotted for reference. Note that the NLNM corresponds to the lower envelope of seismic PSDs computed at that time, so it represents the lowest noise level reached by seismometers anywhere in the world.

Fifth percentile of PSD noise levels of the eight GWR Superconducting Gravimeters (C026, iOSG23, iGrav6, iGrav15, iGrav29, iGrav30, iGrav31, iGrav32) that were recording at the J9 Gravimetric Observatory of Strasbourg are shown on Fig. 21.

The SGs present the lowest noise magnitude in the seismic band between 10^{-3} and 10^{-2} Hz for gravimeters. However, STS-1 long period seismometers provide lower noise above 1.5×10^{-3} Hz as indicated by the NLNM (Widmer-Schmidrig, 2003). Noise increases at the right part of Fig. 21 because of the microseismic signals. At the high frequency end of the spectrum there is a steep roll-off (drop in amplitude) till the Nyquist frequency of 0.5 Hz because of the built-in low pass anti-aliasing filters of the SGs. Some individual lines sticking out of the noise are the so-called parasitic modes of the SG (Imanishi, 2009).

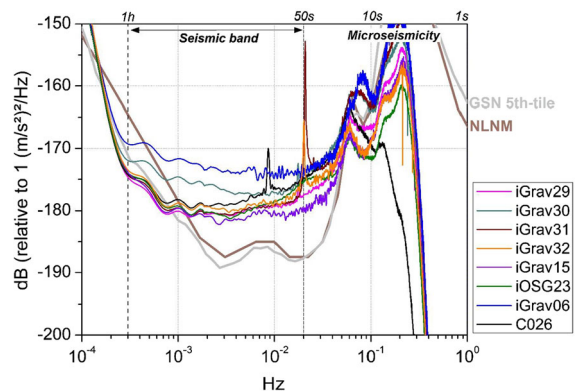


Figure 21

Fifth percentile of PSD noise levels computed on 1-s sampling data of the eight GWR Superconducting Gravimeters (C026, iOSG23, iGrav6, iGrav15, iGrav29, iGrav30 and iGrav31 and iGrav32) that were recording at the J9 Gravimetric Observatory of Strasbourg (France). The new low noise model (NLNM) of Peterson (1993) is represented by the thick brown line. In solid gray lines, we have plotted the 5th percentile of the PSD levels obtained by Berger et al. (2004) for the Global Seismographic Network (GSN 5th-tile)

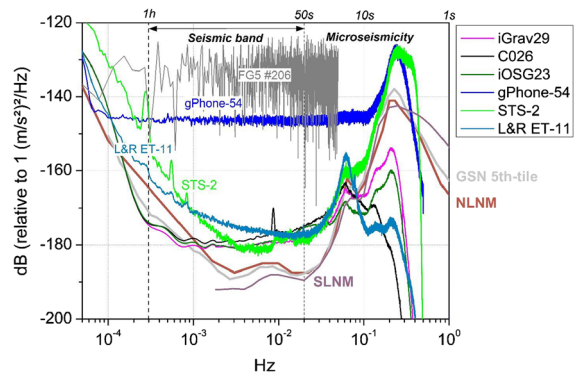


Figure 22

Fifth percentile of PSD noise levels computed on 1-s sampling data of the 3 GWR Superconducting Gravimeters (C026, iOSG23, iGrav29), of the STS-2 seismometer, of the Micro-g LaCoste gPhone-54 and of the LaCoste and Romberg ET-11 gravimeter that were recording at the J9 Gravimetric Observatory of Strasbourg (France). The FG5#206 drop files were also used to compute the corresponding PSD. The New Low Noise Model (NLNM) of Peterson (1993) is represented by the thick brown line and the SLNM of Castellaro and Mulargia (2012) is represented by the thick dashed pink line. In gray lines, we have plotted the 5th percentile of the PSD levels obtained by Berger et al. (2004) for the Global Seismographic Network (GSN 5th-tile). Figure modified from Rosat and Hinderer (2018)

The excellent agreement between the noise levels of six of the eight SGs as shown in Fig. 21 is one of the most important results of this study. Indeed the noise levels of C026, iOSG23 and iGravs 15, 29, 31

and 32 all agree within a few dB (relative to $1 \text{ (m/s}^2\text{)}^2\text{/Hz}$) in the seismic band. From this result, we conclude that the various pillar designs used at J9 and shown in Fig. 1 do not significantly affect the noise of the SGs. Mounting an iGrav directly on the floor operates as quietly as an SG installed on an isolated pillar. In addition, the noise levels of the iGravs and iOSG match that of the older Compact C026, so the performance of the iGravs remains equal to previous SGs.

In contrast, we observe that the noise levels of two iGravs (iGrav30 and iGrav6) are significantly higher (5 db and 8 db) than the other six SGs. The auxiliary channels show that both the tilt noise and dewar pressure noise are 15 dB higher for iGrav30 than for iGrav31. This was later diagnosed as caused by a faulty pressure sensor in the head of the dewar leading to a tension of the vibration isolation diaphragm larger than nominal and hence transmitting coldhead and tilt noise to the gravity sensor; this pressure sensor was replaced before iGrav30 was moved to Strengbach. And, the iGrav06 was installed during the shortest time-period (~ 25 days) in which several earthquakes occurred. Since we have picked the 5th tile among these 25 days, it is more difficult to obtain quiet days in such a short time window. For other SGs, we have picked up the 5th-tile among at least 100 daily PSDs. Because the iOSG23, C026 and iGrav instruments are located in a similar environment, differences in the observed noise levels can be investigated by extracting the coherent and incoherent noise from the observed noise. We refer to the work by Rosat et al. (2015) and Rosat and Hinderer (2018) for detailed comparisons of SG noise levels with other spring gravimeters (ET-11, gPhone-054), a STS-2 seismometer and the absolute gravimeter FG5#206 recording at J9.

iGrav30 and iGrav6 provide a note of caution to all users of iGravs, SGs and other scientific instruments that are designed to operate for years to decades. It is wise to periodically check the performance of SGs to make sure they are meeting their noise specifications rather than wait until the end of a project to analyze data and then find problems that interfere with the project goals. Checking the noise levels is very easy with iGravs that were designed compatible to TSoft (Van Camp & Vauterin, 2005)

and feature software can be set up to reassure users that all is well, or to warn of pending instrumental problems. It is highly recommended that all users of iGravs activate the data system feature that automatically send emails to the user(s) that include both a summary table of operating variables and a short TSoft file. The TSoft file is automatically calculated at the end of the day and a GWR_’summaryScript’ (iGrav User’s Guide, 2019). This summaryScript immediately provides the daily residual and temporal noise throughout the day and can easily be edited by the user.

For the sake of completeness, we have plotted in Fig. 22 the fifth percentile of PSD noise levels of SGs together with other spring gravimeters (ET-11, gPhone-054), the STS-2 seismometer and the absolute gravimeter FG5#206. For this meter we used drop measurements performed every 10 s. Each drop corresponds to one free fall of the test mass. In Rosat et al. (2015), the PSD for the FG5 was computed on set values at an hourly sampling with a noise level of -125 dB at 10^{-4} Hz. Here we can see that using 10-s drop values, we have slightly reduced the noise level to around -130 dB. This level is still the largest of all meters in the seismic band and comes from the fact that absolute measurements are contaminated by aliased microseismic noise (see e.g. Crossley et al., 2001) which explains the rather flat FG5 noise spectrum. A similar aliasing is observed in the gPhone-54 PSD.

The spring relative meters have lower noise levels than the FG5#206 and range from -145 dB for the gPhone-54 to -175 dB for ET-11 and the STS-2 seismometer.

At higher frequencies, the STS-2 shows similar performances like the SGs. At sub-seismic frequencies (below 10^{-3} Hz), the SGs show lowest noise levels; while the ET-11 spring gravimeter noise is 10 dB higher and the gPhone is 30 dB higher. We refer to the work by Rosat et al. (2015) for detailed comparisons and self-noise analysis for these instruments. In the following we only focus on the SGs and their instrumental performances.

5.2. Self-Noise Levels

The observed noise level for an instrument at a site consists of the Earth's environmental background noise (containing all geophysical processes) and the instrumental noise, including the noise coming from the digital acquisition system and the electronics and some possible effects of the physical installation itself (e.g. placement in a building, or an installation directly on the building floor or on a pillar isolated from the building vibrations). In order to separate the instrumental noise from the ambient noise, Sleeman et al. (2006) have proposed a three-channel correlation analysis. Compared to a two-channel analysis, this technique has the advantage that we do not need to know the transfer functions of the instruments. The main assumption is that the internal noise between two channels is uncorrelated to each other and to the common input signal. The self-noise power spectral density of channel i can hence be written as:

$$N_{ii} = P_{ii} - P_{ji}P_{ik}/P_{jk}, \quad (2)$$

where P_{ii} is the PSD of channel i , and P_{ji} (respectively P_{ik} , P_{jk}) is the cross-PSD between channels j and i (i and k , j and k). The equation for self-noise PSD can also be expressed as:

$$N_{ii} = P_{ii}(1 - C_{ji}C_{ik}/C_{jk}), \quad (3)$$

where C_{ji} (respectively C_{ik} , C_{jk}) is the coherency between channels j and i (i and k , j and k). The noise cross-power spectra N_{ij} (resp. N_{ik} , N_{jk}) of internal noise for channels i and j (i and k , j and k) are assumed to be zero for $i \neq j$ ($i \neq k$, $j \neq k$). According to these conventions, the instrumental self-noise will be defined by N_{ii} and the common geophysical noise viewed by the instruments is represented by $P_{ii} - N_{ii}$.

In order to apply the three-channel correlation analysis of Sleeman et al. (2006), we compute the PSDs and the cross-PSDs of the various calibrated SG records using a modified Welch periodogram method applied by averaging 9 segments of 48-h SG time-windows overlapped by 75% on two selected time-periods of 15 days. Two time-periods, April 8–23, 2017 and August 10–25, 2017 were selected because of the joint availability of records from at

least three instruments free of disturbances due to human intervention.

Theoretically, the noise of the SG sensor is due to the thermal noise associated with Brownian motion of the levitating sphere. The expression of the power spectral density of a damped harmonic oscillator due to Brownian motion can be written as (Richter et al., 1995; Aki & Richards, 2009eqn. 12.40):

$$P_{thermal} = 4k_B T \frac{\omega_0}{mQ}, \quad (4)$$

where ω_0 is the natural angular frequency of the oscillator, Q its quality factor and m is the mass of the oscillating sphere; k_B is the Boltzmann constant and T the absolute temperature within the sensor. When there is no difference in the noise characteristics between three instruments (if instruments are equally installed at the same site for instance), the self-noise should be well explained by the thermal noise model.

In Eq. (4) we use the Q value of the magnetic levitation system of the SG modeled as a mechanical damped oscillator. The measured Q value (Table 10) is low (0.109 for iOSG23 and 0.055 for iGrav29) because the sphere's motion is strongly damped by eddy currents in the non-superconducting materials in the sensor (in the nearby Al plates and in the magnet form). This damping is much larger than that caused by the viscous drag on the sphere moving in the surrounding helium gas. Moreover there are other noise sources that include temperature control noise, tilt noise, electronic noise, noise from the boiling He, coldhead vibrations, and digitization noise; some of which are difficult to quantify. However these noise sources seem below the thermal noise of the iGrav as is discussed hereafter.

The parameters that are needed to compute the thermal noise PSD of iGrav29 and iOSG23 are given in Table 10.

The three-channel correlation analysis was already applied by Rosat et al. (2015) on the STS-2 seismometer, the LaCoste-Romberg ET-11 gravimeter and the SG C026 recording at J9. Because of different band-pass frequencies and different digital acquisition system (DAS), it was however not possible to extract the sensor noise from the noise of the DAS. Here, we have the possibility to evaluate the sensor noise since the DAS used for every iGrav

Table 10

Harmonic oscillator parameter values used in Eq. 4 to compute the spectral acceleration-noise power density due to Brownian motion

Parameter	Unit	iGrav29	iOSG23
Mass m	kg	$4.02 \cdot 10^{-3}$	$17.7 \cdot 10^{-3}$
Frequency f_0	Hz	0.238	0.105
Q		0.109	0.055
Spring constant k	N/m	0.0090	0.0077
Damping factor b	kg/s	0.055	0.214
Mean PSD	dB	-181	-188

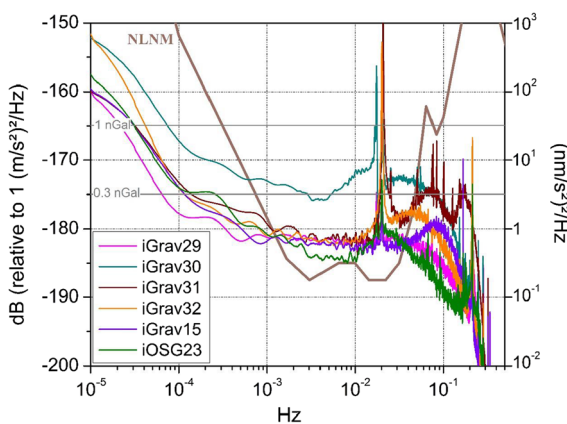


Figure 23

Results of the three-channel correlation analysis applied on the 1-s data for iGrav30 and iGrav31 and iOSG23 on the 15-day time period 2017, April 8th to 23rd and for iGrav32, iGrav29 and iGrav15 on the 15-day time period between 2017, August 10th and 25th. Common noise was removed by this method and only self-noise PSDs are plotted

and for the iOSG23 is identical. A similar study was already done in Rosat and Hinderer (2018) but on a more limited number of iGrav instruments.

The results of the three-channel correlation analysis applied to the iGravs and the iOSG recording at J9 are shown in Fig. 23. We can see that at seismic frequencies higher than 1 mHz and lower than the start of the roll-off due to the low-pass anti-aliasing filter, the thermal noise model (-181 dB, Table 10) agrees well with the extracted self-noise PSD for iGravs with a difference of a few dB (< 5 dB), except for iGrav30, which had a problem due to a faulty dewar pressure sensor previously discussed in Sect. 4.2 and previously shown in

Fig. 21. The close matching of the thermal noise to the observed noise of the SG simply means that other noise sources of the SG are below its thermal noise.

Because of its heavier levitated sphere, the thermal noise for iOSG23 should be just below the NLNM seismic noise and a few decibels lower than the thermal noise of iGrav instruments (-188 dB, Table 10).

The fact that the self-noise of iOSG23 results to be about 5 dB larger than its thermal noise model in the seismic band (mHz frequency range) is likely due to additional noise sources previously mentioned. That the iOSG noise is lower than the iGrav self-noise is likely the influence of its larger mass in agreement with Eq. (4). We also point out that the thermal noise of the STS1 long-period seismometer is lower than that of the SG, and that this also is likely due to its mass being much larger (600 g) and perhaps its lower damping (Richter et al., 1995).

We can see that the self-noise for iGrav15 and 32 which were installed directly on the ground are similar to the one of the iOSG23 at periods larger than 1 h and similar to the one of iGrav29 at seismic frequencies. We conclude that the variations in physical installations at J9 did not significantly affect the noise levels and that installation on the concrete ground is as good as on a small or large isolated pillar.

Two parasitic noise peaks around $2 \cdot 10^{-2}$ Hz (one at 57 s for iGrav30 and one at 48 s for iGrav29 and iGrav31) are visible in the PSDs (Fig. 23). These vibrations correspond to the low-frequency parasitic mode (Richter et al., 1995; Van Camp, 1999) due to horizontal displacements of the sphere that turn into an orbital mode (Hinderer et al., 2015). For iGrav32, this mode appears at 20 mHz (Schäfer et al., 2020). Peaks at 0.24 Hz and harmonics may be due to some other parasitic modes associated with other degrees of freedom of the sphere (Imanishi, 2009), coldhead noise, or other unidentified effects.

6. Conclusion

Superconducting gravimeters (SG) are currently the most sensitive relative gravimeters with the lowest drift rates which, as demonstrated in our study,

can be modelled and reduced with the help of absolute gravity measurements. Therefore, these sensors are particularly suitable for studying a wide range of geophysical processes which induce weak gravity effects over time intervals of minutes to years.

We compared in detail eight SGs located inside the Strasbourg Gravimetric Observatory including five of the latest generation of field SGs, the so-called iGravs, one iOSG with a heavier sphere and an older compact meter C026. The calibration of the instruments was investigated both in an absolute way, by parallel absolute measurements, as well as in a relative way by computing the regression between parallel SG time series. We found out that relative calibration determined from different SGs at the same site can be much more precise than absolute calibration. We could also demonstrate that using relative scale factors strongly reduces the tidal residuals between two different SGs which is not the case when using absolute calibration.

We checked the instrumental time delays (phase lag) of the various SGs from cross-correlation analysis between different parallel time series. All the iGravs have similar time delays of a few seconds with respect to iOSG23. Moreover, the time delays for a specific gravimeter inferred from a one year long tidal analysis, step experiments and time regression were all found to agree.

We discussed the instrumental drift of the SGs and found that all the meters exhibit an initial exponential drift best approximated by two exponentials with different time constants, followed by a long-term linear drift. We could also show the consequences of the initialization/levitation procedures on the instrumental drift, especially for iGrav29 that was used as test instrument in this study. A rather strong correlation was found between the gravity drift and the body-temperature signal but it is not a straightforward or linear relationship.

Furthermore, we have performed a noise level analysis of all the iGravs and the iOSG23. A three-channel correlation technique was applied to identify the common noise and the self-noise of the various iGravs and the iOSG. However, small differences in self noise are not caused by the installation method (on concrete pillars or directly on the floor) or

instrumental configurations; but they may be caused by differences in their transfer functions.

Small differences in self-noise could possibly be interpreted in terms of local noise effects that are incoherent between the various instruments separated by a few meters. For example, lateral contrast in local soil moisture in the loess layer above the Observatory could lead to slightly different signals of each gravimeter.

The present metrological study is of importance for several geophysical applications. A good knowledge of the instrumental drift is essential for the study involving long-period gravity changes. We can mention for instance the difficulty of separating post-glacial rebound effects from present-day ice-melting where the combination of AG and SG observations helped considerably to reduce the uncertainty in the AG estimated decrease due to ice melting in Svalbard (Memin et al. 2014). Furthermore, studies on slow recharge processes in magma chambers could benefit greatly from a thorough knowledge of the drift of the gravimeters used to monitor active volcanoes (Okubo, 2020; Riccardi et al., 2008). Knowledge of the purely instrumental noise and separation from environmental noise can help to detect small signals which are hidden in the overall noise (e.g. Rosat & Hinderer, 2018). Accurate calibration of the SGs is essential for the determination of tidal amplitudes and phases that is fundamental for tidal tomography and investigation of lateral heterogeneity effects (Metivier et al. 2007; Latychev et al., 2009).

Acknowledgements

We thank Y. Imanishi and W. Zuern for their careful reviews of this manuscript and the technical discussions they raised. The iOSG23 gravimeter at J9 gravimetric observatory was funded by the EQUIPEX RESIF-CORE. The iGravs #29, #30 and #31 were funded by the EQUIPEX CRITEX. The authors are grateful to R. Reineman from GWR Inc. for the installation of the iOSG23 and the iGravs. The Micro-g LaCoste Inc. gPhone-054 with the PET (Portable Earth Tide gravimeter) system was kindly lent by the Instituto Geografico Nacional (IGN) of Madrid in Spain. The authors thank also Dr. Marta

Calvo for helping in the installation of the meter. We acknowledge W. Zürn from Black Forest Observatory who had temporarily installed the LaCoste-Romberg ET-11 in J9. Continuous support of INSU-CNRS to operate the Strasbourg Gravimetry Observatory is acknowledged. Data from the SG C026 and iOSG23 are available from IGETS <http://doi.org/10.5880/igets.st.11.001>.

Publisher's Note Springer Nature remains neutral with regard to jurisdictional claims in published maps and institutional affiliations.

REFERENCES

- Aki, K., & Richards, P. (2009). *Quantitative seismology, second edition, 2009* (p. 700). University Science Books.
- Amalvict, M., Hinderer, J., Boy, J.-P., & Gegout, P. (2001). A three year comparison between a superconducting gravimeter (GWR C026) and an absolute gravimeter (FG5#206) in Strasbourg (France). *Journal of the Geodetic Society of Japan*, 47, 334–340.
- Arnosó, J., Riccardi, U., Hinderer, J., Córdoba, B., & Montesinos, F. G. (2014). Analysis of co-located measurements made with a LaCoste & Romberg Graviton-EG gravimeter and two superconducting gravimeters at Strasbourg (France) and Yebes (Spain). *Acta Geodaetica Geophysica*, 49, 147–160. <https://doi.org/10.1007/s40328-014-0043-y>
- Berger, J., Davis, P., & Ekström, G. (2004). Ambient earth noise: A survey of the global seismographic network. *Journal of Geophysical Research*, 109, B11307.
- Boy, J.-P., Rosat, S., Hinderer, J., & Littel, F. (2017). Superconducting gravimeter data from Strasbourg—level 1. *GFZ Data Services*. <https://doi.org/10.5880/igets.st.11.001>
- Calvo, M., Rosat, S., Hinderer, J. (2016). Tidal spectroscopy from a long record of superconducting gravimeters in Strasbourg (France). International Associations of Geodesy Symposia, Prague (Czech Rep.)., Berlin, Heidelberg: Springer. https://doi.org/10.1007/1345_2016_223
- Calvo, M., Hinderer, J., Rosat, S., Legros, H., Boy, J.-P., Ducarme, B., & Zürn, W. (2014). Time stability of spring and superconducting gravimeters through the analysis of very long gravity records. *Journal of Geodynamics*, 80, 20–33. <https://doi.org/10.1016/j.jog.2014.04.009>
- Calvo, M., Hinderer, J., Rosat, S., Legros, H., Boy, J.-P., Ducarme, B., & Zürn, W. (2017). Corrigendum to “Time stability of spring and superconducting gravimeters through the analysis of very long gravity records” [J. Geodyn. 80, (2014) 20–33]. *Journal of Geodynamics*, 106, 30–32. <https://doi.org/10.1016/j.jog.2017.01.007>
- Castellaro, S., & Mulargia, F. (2012). A statistical low noise model of the earth. *Seismological Research Letters*, 83(1), 39–48. <https://doi.org/10.1785/gssrl.83.1.39>
- Chaffaut, Q., Hinderer, J., Masson, F., Viville, D., Bernard, J.-D., Cotel, S., Pierret, M.-C., Lesparre, N., and Jeannot, B., (2020). Continuous monitoring with a superconducting gravimeter as a proxy for water storage changes in a mountain catchment, in *IAG symposia series, Proceedings of IUGG 27th general assembly, Montreal, Canada, International Association of Geodesy symposia*, https://doi.org/10.1007/1345_2020_105
- Crossley, D., Calvo, M., Rosat, S., & Hinderer, J. (2018). *More thoughts on AG–SG comparisons and SG scale factor determinations*. *Geophysics*. <https://doi.org/10.1007/s00024-018-1834-9>
- Crossley, D., Hinderer, J., & Amalvict, M. (2001). A spectral comparison of absolute and superconducting gravimeter data. *Journal of the Geodetic Society of Japan*, 47, 373–379.
- Crossley, D., Hinderer, J., & Boy, J.-P. (2004). Regional gravity variations in Europe from superconducting gravimeters. *Journal of Geodynamics*, 38, 325–342.
- Ducarme, B. & Schüller, K., (2018). Canonical wave grouping as the key tool for optimal tidal analysis, Bulletin d'Informations Mares Terrestres (BIM), No. 150: 12131-12244. ISSN: 0542-6766, <http://www.bim-icet.org/>
- Dykowski P., Krynski J., Sękowski M., (2019): A 3 year long AG/SG gravity time series at Borowa Gora Geodetic Geodetic-Geophysical Observatory, 27 IUGG General Assembly 2019, Montreal, Canada, 08–18 July 2019.
- Erbaş, K., F. Schäfer, Á. Guðmundson, E. Júlíusson, G. Hersir, R. Warburton, J.-D. Bernard, N. Portier, J. Hinderer, V. Drouin, F. Sigmundsson, K. Ágústsson, B. Männel, A. Güntner, C. Voigt, T. Schöne, A. Jolly, H. Hjartasson, D. Naranjo, P. Jousset, (2019). Continuous microgravity monitoring in a volcanic geothermal field: Integrated observational approach in Þeistareykir, NE Iceland, in *Proceedings World geothermal congress 2020, Reykjavik, Iceland, April 26–May 2, 2020, accepted*.
- Fukuda, Y., Iwano, S., Ikeda, H., Hiraoka, Y., & Doi, K. (2005). Calibration of the superconducting gravimeter CT#043 with an absolute gravimeter FG5#210 at Syowa Station, Antarctica. *Polar Geoscience*, 18, 41–48.
- Gaillardet, J., et al. (2018). OZCAR: The French network of critical zone observatories. *Vadose Zone Journal*, 17, 180067. <https://doi.org/10.2136/vzj2018.04.0067>
- Hinderer, J., Crossley, D., & Warburton, R. (2015). Superconducting gravimetry. In T. Herring & G. Schubert (Eds.), *Treatise on Geophysics, Geodesy* (2nd ed., Vol. 3, pp. 66–122). Amsterdam: Elsevier.
- Hinderer, J., Florsch, N., Mäkinen, J., Legros, H., & Faller, J. E. (1991). On the calibration of a superconducting gravimeter using absolute gravity measurements. *Geophysical Journal International*, 106, 491–497.
- iGrav User's Guide, (2019). GWR Instruments, Inc. (Revision 4.01). San Diego, USA.
- Imanishi, Y. (2009). High-frequency parasitic modes of superconducting gravimeters. *Journal of Geodesy*, 83, 455–467.
- Imanishi, Y., Higashi, T., & Fukuda, Y. (2002). Calibration of the superconducting gravimeter T011 by parallel observation with the absolute gravimeter FG5 #210—a Bayesian approach. *Geophysical Journal International*, 151, 867–878.
- Latychev, K., Mitrovica, J. X., Ishii, M., Chan, N.-H., & Davis, J. L. (2009). Body tides on a 3-D elastic earth: Toward a tidal tomography. *Earth and Planet Science Letters*, 277, 86–90.
- Mémin, A., Spada, G., Jean-Paul Boy, Y., & Rogister, & J. Hinderer., (2014). Decadal geodetic variations in Ny-Ålesund (Svalbard): role of past and present ice-mass changes. *Geophysical Journal International*, 198(1), 285–297. <https://doi.org/10.1093/GJI/GGU134>

- Metivier, L., Greff-Lefftz, M., & Diament, M. (2007). Mantle lateral variations and elastogravitational deformations—II. Possible effects of a superplume on body tides. *Geophysical Journal International*, 168, 897–903.
- Meurers, B. (2012). Superconducting gravimeter calibration by collocated gravity observations: Results from GWR C025. *International Journal of Geophysics*, 2012, 12.
- Mouyen, M., Longuevergne, L., Chalikakis, K., Mazzilli, N., Ollivier, C., Rosat, S., Hinderer, J., & Champollion, C. (2019). Monitoring of groundwater redistribution in a karst aquifer using a superconducting gravimeter. *E3S Web of Conference*, 88, 03001. <https://doi.org/10.1051/e3sconf/20198803001>
- Okubo, S. (2020). Advances in gravity analyses for studying volcanoes and earthquakes. *Proceedings of the Japan Academy, Series B*. <https://doi.org/10.2183/pjab.96.005>
- Peterson, J. (1993). Observations and modelling of seismic background noise. Open-File Report 93-332. U. Department of Interior, Geological Survey, Albuquerque, New Mexico.
- Riccardi, U., Berrino, G., Corrado, G., & Hinderer, J. (2008). Strategies in the processing and analyses of continuous gravity record in active volcanic areas: The case of Mt. Vesuvius. *Annals of Geophysics*, 51, 67–85.
- Riccardi, U., Hinderer, J., Boy, J.-P., & Rogister, Y. (2009). Tilt effects on GWR superconducting gravimeters. *Journal of Geodynamics*, 48, 316–324. <https://doi.org/10.1016/j.jog.2009.09.001>
- Riccardi, U., Rosat, S., & Hinderer, J. (2011). Comparison of the Micro-g LaCoste gPhone-054 spring gravimeter and the GWR-C026 superconducting gravimeter in Strasbourg (France) using a 300-day time series. *Metrologia*, 48, 28–39.
- Riccardi, U., Rosat, S., & Hinderer, J. (2012). On the accuracy of the calibration of superconducting gravimeters using absolute and spring sensors: A critical comparison. *Pure and Applied Geophysics*, 169(8), 1343–1356.
- Richter, B., Wenzel, H.-G., Zürn, W., & Klopping, F. (1995). From Chandler wobble to free oscillations: Comparison of cryogenic gravimeters and other instruments in a wide period range. *Physics of the Earth and Planetary Interiors*, 91, 131–148.
- Rosat, S., Boy, J.-P., Ferhat, G., Hinderer, J., Amalvict, M., Gegout, P., & Luck, B. (2009). Analysis of a ten-year (1997–2007) record of time-varying gravity in Strasbourg using absolute and superconducting gravimeters: New results on the calibration and comparison with GPS height changes and hydrology. *Journal of Geodynamics*, 48, 360–365. <https://doi.org/10.1016/j.jog.2009.09.026>
- Rosat, S., Calvo, M., Hinderer, J., Riccardi, U., Arnos, J., & Zürn, W. (2015). Comparison of the performances of different spring and superconducting gravimeters and a STS-2 seismometer at the Gravimetric Observatory of Strasbourg, France. *Studia Geophysica Et Geodaetica*, 59, 58–82. <https://doi.org/10.1007/s11200-014-0830-5>
- Rosat, S., & Hinderer, J. (2011). Noise levels of superconducting gravimeters: Updated comparison and time stability. *Bulletin of the Seismological Society of America*, 101(3), 1233–1241.
- Rosat, S., & Hinderer, J. (2018). Limits of detection of gravimetric signals on Earth. *Scientific Reports*. <https://doi.org/10.1038/s41598-018-33717-z>
- Rosat, S., Hinderer, J., Boy, J.-P., Littel, F., Bernard, J.-D., Boyer, D., Mémin, A., Rogister, Y., & Gaffet, S. (2018). A two-year analysis of the iOSG-24 superconducting gravimeter at the low noise underground laboratory (LSBB URL) of Rustrel, France: Environmental noise estimate. *Journal of Geodynamics*, 119, 1–8. <https://doi.org/10.1016/j.jog.2018.05.009>
- Rosat, S., Hinderer, J., Boy, J.-P., Littel, F., Boyer, D., Bernard, J.-D., Rogister, Y., Mémin, A., & Gaffet, S. (2016). First analyses of the iOSG-type superconducting gravimeter at the low noise underground laboratory (LSBB URL) of Rustrel, France. *E3S Web of Conference*, 12, 06003. <https://doi.org/10.1051/e3sconf/20161206003>
- Schäfer, F., Jousset, P., Güntner, A., Erbas, K., Hinderer, J., Rosat, S., Voigt, C., Schöne, T., & Warburton, R. (2020). Performance of three iGrav superconducting gravity meters before and after transport to remote monitoring sites. *Geophysical Journal International*, 223(2), 959–972. <https://doi.org/10.1093/gji/ggaa359>
- Schüller, K., (2018). Theoretical basis for earth tide analysis and prediction manual-01-ET34-X-V71, Surin, Thailand, p. 217.
- Sleeman, R., van Wettum, A., & Trampert, J. (2006). Three-channel correlation analysis: A new technique to measure instrumental noise of digitizers and seismic sensors. *Bulletin of the Seismological Society of America*, 96(1), 258–271.
- Tamura, Y., Sato, T., Fukuda, Y., & Higashi, T. (2004). Scale factor calibration of a superconducting gravimeter at Esashi Station, Japan, using absolute gravity measurements. *Journal of Geodesy*, 78(7–8), 481–488. <https://doi.org/10.1007/s00190-004-0415-0>
- Van Camp, M. (1999). Measuring seismic normal modes with the GWR C021 superconducting gravimeter. *Physics of the Earth and Planetary Interiors*, 116, 81–92.
- Van Camp, M., & Francis, O. (2007). Is the instrumental drift of superconducting gravimeters a linear or exponential function of time? *Journal of Geodesy*, 81(5), 337–344. <https://doi.org/10.1007/s00190-006-0110-4>
- Van Camp, M., Meurers, B., de Viron, O., & Forbriger, T. (2015). Optimized strategy for the calibration of superconducting gravimeters at the one per mille level. *Journal of Geodesy*, 90(1), 91–99. <https://doi.org/10.1007/s00190-015-0856-7>
- Van Camp, M., & Vauterin, P. (2005). Tsoft: Graphical and interactive software for the analysis of time series and Earth tides. *Computers and Geosciences*, 31(5), 631–640. <https://doi.org/10.1016/j.cageo.2004.11.015>
- Van Camp, M., Wenzel, H.-G., Schott, P., Vauterin, P., & Francis, O. (2000). Accurate transfer function determination for superconducting gravimeters. *Geophysical Research Letters*, 27(1), 37–40.
- Warburton, R. (1997). Optimizing the performance of the SG during the GGP. First GGP Workshop, 21 July 1997, Brussels, Belgium.
- Warburton, R. J., Pillai, H., & Reineman, R. C. (2011). Initial results with the new GWR iGrav superconducting gravity meter. In: Proceedings of the IAG symposium on terrestrial gravimetry: Static and mobile measurements (TG-SMM2010), 22–25 June 2010, Russia, Saint Petersburg, 138.
- Welch, P. (1967). The use of fast Fourier transform for the estimation of power spectra: A method based on time averaging over

short, modified periodograms. *IEEE Transactions on Audio and Electroacoustics*, 15(2), 70–73. <https://doi.org/10.1109/tau.1967.1161901>

Widmer-Schmidrig, R. (2003). What can superconducting gravimeters contribute to normal-mode seismology? *Bulletin of the Seismological Society of America*, 93(3), 1370–1380. <https://doi.org/10.1785/0120020149>

(Received July 1, 2021, revised March 1, 2022, accepted March 6, 2022, Published online April 21, 2022)